Calibration of the dual clumped isotope thermometer for carbonates

Jens Fiebig [a,*], Mathieu Daëron [b], Miguel Bernecker [a], Weifu Guo [c], Gaby Schneider [d], Ronny Boch [e], Stefano M. Bernasconi [f], Josue Jautzy [g], Martin Dietzel [e]

[a] *Institut für Geowissenschaften, Goethe Universität, Altenhöferallee 1, 60438 Frankfurt am Main, Germany*
[b] *Laboratoire des Sciences du Climat et de l'Environnement, LSCE/IPSL, CEA-CNRS-UVSQ, Université Paris-Saclay, Orme des Merisiers, F-91191 Gif-sur-Yvette, France*
[c] *Department of Geology and Geophysics, Woods Hole Oceanographic Institution, Woods Hole, MA 02543, United States*
[d] *Institut für Mathematik, Goethe Universität, Robert-Mayer Straße 10, 60325 Frankfurt am Main, Germany*
[e] *Institut für Angewandte Geowissenschaften, Technische Universität Graz, Rechbauerstraße 12, 8010 Graz, Austria*
[f] *Department of Earth Sciences, ETH Zürich, Sonneggstrasse 5, 8092 Zürich, Switzerland*
[g] *Geological Survey of Canada, Natural Resources Canada, 490 De la Couronne Street, Québec City, Québec G1K 9A9, Canada*

Abstract

The Δ_{47} (paleo)thermometer has opened a new avenue to determine carbonate formation temperatures independent of the oxygen isotopic composition of the fluid from which the carbonate crystallized. A major limitation of this thermometer is related to kinetic effects if homogeneous isotopic equilibrium is not attained during carbonate precipitation. Dual clumped isotope thermometry – the high-precision analysis of Δ_{48} along with Δ_{47} in CO_2 evolved from phosphoric acid digestion of carbonates – makes it possible to resolve temperature from the kinetic information recorded in an individual carbonate phase. Therefore, it provides a new opportunity to identify (bio)mineralization pathways and to determine carbonate formation temperatures devoid of a kinetic bias, based solely on isotopic analysis of a single carbonate phase.

Identification of the nature and extent of kinetic effects as well as the reconstruction of accurate formation temperatures requires knowledge of the position of equilibrium in Δ_{47} vs Δ_{48} space. Here, we present Δ_{47} and Δ_{48} data of carbonates that were previously considered as having crystallized closest to equilibrium in a temperature range of 8 to 1100 °C. Across this range, the temperature dependences of Δ_{47} and Δ_{48} are best expressed by the following fourth order polynomials of $1/T$:

Δ_{47} (CDES 90) (‰) = 1.038 (-5.897 $1/T$ $-$ 3.521 10^3 $1/T^2$ + 2.391 10^7 $1/T^3$ $-$ 3.541 10^9 $1/T^4$) + 0.1856
Δ_{48} (CDES 90) (‰) = 1.028 (6.002 $1/T$ $-$ 1.299 10^4 $1/T^2$ + 8.996 10^6 $1/T^3$ $-$ 7.423 10^8 $1/T^4$) + 0.1245

with CDES 90 representing the Carbon Dioxide Equilibrium Scale at a reaction temperature of 90 °C. In its entire temperature range, our Δ_{47} (CDES 90) - T - relationship agrees within 2 ppm with two previous Δ_{47} (I-CDES) - T - relationships reported by Jautzy et al. (2020) and Anderson et al. (2021). Accuracy of our proposed Δ_{47} (CDES 90) $-$ Δ_{48} (CDES 90) equilibrium relationship is independently confirmed by additional dual clumped isotope data of experimental and geothermal carbonates which precipitated from potentially equilibrated dissolved inorganic carbon pools at a temperature range of 25–100 °C. Furthermore, we reprocessed original dual clumped isotope data of natural carbonates (Bajnai et al., 2020) and compared their composition to the position of equilibrium in Δ_{47} vs Δ_{48} space. These results corroborate preliminary evidence that the hydration/hydroxylation reactions became rate-limiting during the calcification of a speleothem-like sample, a warm water coral, a cold water coral and a brachiopod, finally evoking significant departures of carbonate-Δ_{47} and -Δ_{48} from dual clumped isotope equilibrium.

* Corresponding author.
  E-mail address: Jens.Fiebig@em.uni-frankfurt.de (J. Fiebig).

An anti-clumped Δ_{48} value of -419 (± 16) ppm (95% confidence interval level) is obtained for a technical calcite that was precipitated by the injection of CO_2 into a $Ca(OH)_2$-saturated solution. Its negative Δ_{48} value largely arises from a combinatorial effect, i.e. the carbonate oxygen derives from two sources with different bulk isotopic compositions. Besides the identification of the nature and the extent of (bio)mineralization kinetics and the reconstruction of carbonate formation temperatures unbiased by kinetics, dual clumped isotope analysis, therefore, allows tracing the isotopic heterogeneity of oxygen pools contributing to carbonate formation.

1. INTRODUCTION

Element abundance ratios (e.g., Mg/Ca in marine carbonates; Nürnberg et al., 1996), organic molecular biomarker compositions (e.g., TEX$_{86}$ in sedimentary organic matter; Schouten et al., 2002) and bulk isotopic compositions (e.g., oxygen isotopic composition of marine carbonates; Urey, 1947; Epstein et al., 1953) of sedimentary archive components have been shown to be controlled by the temperature at which their formation takes place. These proxy thermometers have been extensively applied to reconstruct Earth's surface temperature through time. However, in addition to temperature, the chemical and isotopic compositions of sedimentary archives can be controlled by reaction kinetics involved in their formation and by the chemical and/or isotopic composition of the aqueous solutions these archives originated from. Moreover, after their formation and deposition, they can be exposed to secondary, diagenetic processes which may alter their primary chemical and isotopic compositions. These additional processes can introduce large scatter and biases in reconstructed Earth's surface temperatures of up to tens of degrees C (e.g., Veizer and Prokoph, 2015).

In the case of sedimentary carbonates, the establishment of the Δ_{47} clumped isotope proxy (Ghosh et al., 2006) has helped to overcome the uncertainty associated with the unknown isotopic composition of the parent water. The Δ_{47} proxy represents the excess abundance of m/z 47 isotopologues ($^{13}C^{18}O^{16}O$, $^{12}C^{17}O^{18}O$ and $^{13}C^{17}O^{17}O$) relative to a stochastic distribution in CO_2 derived from phosphoric acid digestion of carbonates:

$$\Delta_{47} = R_{47}/R_{47}^* - 1 \tag{1}$$

where R_{47} and R_{47}^* represent the measured and stochastic 47/44 isotopologue ratios, respectively. The Δ_{47} value characterizes the fractionation of isotopes within the individual carbonate phase. In cases where internal isotopic equilibrium is attained within the carbonate, this value depends only on equilibration temperature, independently of the carbon and oxygen isotopic composition of the parent fluid. Beyond its purpose for paleoclimate reconstruction, this single-phase thermometer has enabled determination of i) body temperatures of extinct vertebrates (e.g., Eagle et al., 2011), ii) cooling rates of metamorphic rocks (e.g., Passey and Henkes, 2012), iii) temperatures associated with hydrothermal, diagenetic and metamorphic formation of extraterrestrial and terrestrial carbonates (Guo and Eiler, 2007; Bristow et al., 2011; Huntington et al., 2011; Passey

and Henkes, 2012). Yet, early experimental and empirical studies yielded different temperature dependencies of Δ_{47} (e.g., Ghosh et al., 2006; Dennis and Schrag, 2010; Petersen et al., 2019). Even when calibration data is reprocessed with the IUPAC ^{17}O parameters as recommended by Daëron et al. (2016) and with a single temperature dependence of the acid fractionation factor, the absolute spread in Δ_{47} at ambient temperatures is still as large as $\pm 0.04‰$ (Petersen et al., 2019). Some investigations implied that kinetics occurring in the solution (diffusion, (de)hydration and (de)hydroxylation reactions) prior to carbonate precipitation and/or at the solution-carbonate interface may introduce at least some of the observed scatter in Δ_{47} (Daëron et al., 2011; Saenger et al., 2012; Bajnai et al., 2018, Guo, 2020). As is the case with oxygen isotopes, species-specific calibrations can only help to overcome the bias introduced by reaction kinetics if the latter are invariable for a given species through time.

Dual clumped isotope thermometry of carbonates, i.e. high-precision analysis of Δ_{48} along with Δ_{47} in CO_2 evolving from phosphoric acid digestion of carbonates, has been postulated (through model data) to allow resolution of temperature from the kinetic information recorded in the single carbonate phase (Guo and Zhou, 2019; Guo, 2020). In analogy to Δ_{47}, the Δ_{48} value is expressed by the excess of mass 48 isotopologues ($^{12}C^{18}O^{18}O$,$^{13}C^{17}O^{18}O$) relative to their stochastic abundances:

$$\Delta_{48} = R_{48}/R_{48}^* - 1 \tag{2}$$

where R_{48} and R_{48}^* represent the measured and stochastic 48/44 isotopologue ratios, respectively. Due to the 10 times lower abundance of $^{12}C^{18}O^{18}O$ relative to $^{13}C^{18}O^{16}O$, Δ_{48}-is even more challenging than Δ_{47}-analysis. Recently, Fiebig et al. (2019) demonstrated that the signal to noise ratio of the 253plus gas source mass spectrometer, equipped with $10^{13}\,\Omega$ amplifiers, is improved by a factor of two if compared to the MAT 253 predecessor, with its $10^{12}\,\Omega$ amplification of the signals recorded on the m/z 47–49 collectors. Using the automated common acid bath purification system HAL, external reproducibilities (1 SD) of ~10 ppm and ~30 ppm, respectively, were achieved for combined Δ_{47} and Δ_{48} measurements on carbonates. A Δ_{48} reproducibility of ~± 30 ppm was observed to be small enough to identify the temperature effect on carbonate Δ_{48} (Fiebig et al., 2019). In a follow-up study, Bajnai et al. (2020) have provided a preliminary estimation of the position of equilibrium in Δ_{47} vs Δ_{48} space which was based on theory and dual clumped isotope data of a slowly

grown natural calcite. To this position they compared the dual clumped isotope compositions of carbonates from a warm-water coral, a cold-water coral, a brachiopod, a belemnite and two speleothems. With the exception of the belemnite, the analyzed carbonates plotted significantly off equilibrium, highlighting the importance of kinetics in carbonate (bio)mineralization. Since the formation temperatures of disequilibrium carbonates were independently known, the magnitudes of kinetic Δ_{47} and Δ_{48} offsets from equilibrium could be determined. The directions and magnitudes of these offsets were consistent with theoretical predictions according to which disequilibrium is introduced in the parent solution by the relatively slow kinetics of the (de)hydration/(de)hydroxylation reactions (Bajnai et al., 2020; Guo, 2020). These reactions are part of the CO_2 absorption and CO_2 degassing sequences, both of which provide important pathways to achieve supersaturation with respect to $CaCO_3$. The corals and the speleothems investigated by Bajnai et al. (2020) exhibited Δ_{47} and Δ_{48} values that are characteristic of the early stages of CO_2 absorption and CO_2 degassing, respectively. In these early stages, the departure from equilibrium occurs along linear trajectories whose slopes are relatively insensitive to temperature and pH (Guo, 2020). Using the theoretically predicted Δ_{47} / Δ_{48} slopes characteristic of CO_2 absorption (−0.6) and CO_2 degassing (−1), the isotopic composition of investigated disequilibrium carbonates could be projected onto the Δ_{47} vs Δ_{48} equilibrium curve to derive carbonate formation temperatures unbiased by kinetics. For the corals and the speleothems, carbonate formation temperatures determined this way were observed to be consistent with real growth temperatures (Bajnai et al., 2020). Dual clumped isotope analyses, therefore, hold great potential to determine accurate carbonate formation temperatures and to identify the nature and extent of (bio) mineralization kinetics.

In order to further explore the potential of dual clumped isotope thermometry for (paleo)temperature reconstruction and the identification of rate-limiting (bio)mineralization reactions, accurate knowledge of the equilibrium position in Δ_{47} vs Δ_{48} space is required. Here, we present a comprehensive dual calibration of equilibrium Δ_{48} and Δ_{47} as a function of temperature, in the range 7.9 °C $\leq$ T $\leq$ 1100 °C. For this purpose, we analyzed a variety of natural, inorganically precipitated and heated carbonates whose (clumped) isotopic compositions were previously considered to represent equilibrium. To test the robustness of our Δ_{47} vs Δ_{48}-temperature calibrations, we compare the dual clumped isotopic compositions of geothermal pipe carbonates, inorganic precipitates and biogenic carbonates (all with known growth temperatures) with the inferred equilibrium Δ_{47} vs Δ_{48}-temperature relationship. The position and trends displayed by these samples in Δ_{47} vs Δ_{48} space are consistent with theoretical expectations, supporting the validity of our Δ_{47} vs Δ_{48} equilibrium relationship.

2. SAMPLES

In order to determine the temperature dependences of Δ_{47} and Δ_{48}, we analyzed the dual clumped isotopic composition of 11 calcite samples (Table 1). It has been postulated in previous studies that heterogeneous and/or homogeneous isotopic equilibrium has been closely attained in these samples. These samples include

(1) Devils Hole calcite, samples DHC2-8 and DVH-2
DCH2-8 represents a 4.5–16.9 kyrs old mammillary calcite that has precipitated at a depth of about 60 m below the water table in the Devils Hole cave #2, southern Nevada, USA. The cave is charged by meteoric waters from the Ash meadows ground water basin. The water temperature inside the cave has remained constant in a range of 32.8–34.3 °C over the last 100 years. Coplen (2007) argued that variations in the Devils Hole calcite $\delta^{18}O$ record can be solely explained by variations in the oxygen isotopic composition of the meteoric water feeding the Ash meadows ground water basin. He, therefore, assumed the latest, directly determined temperatures of 33.7 $\pm$ 0.2 °C (Plummer et al., 2000) to be representative for the growth of DHC2-8. Attainment of equilibrium is consistent with the extremely slow growth rates (0.1–0. 8 μm/yr) of Devils Hole mammillary calcite, the relatively low modern calcite saturation index < 0.2 and the circumneutral pH of 7.4 of the groundwater (the combination of extremely slow growth rates and circumneutral pH are known to be favorable for the attainment of equilibrium; Watkins et al., 2014) and indistinguishable $\delta^{18}O$ of contemporaneously deposited calcite sections (Plummer et al., 2000; Coplen, 2007).
A 0.5 × 0.5 × 1.5 cm slab of DHC2-8 was cut off the original core. Its outermost surface was abraded using a hand-held drill to remove any contamination. The section was cleaned with distilled water in an ultrasonic bath and afterwards dried in a vacuum oven at 30 °C. The material was crushed and homogenized using an agate mortar and pestle and analyzed for its dual clumped isotopic composition within three different analytical sessions, including a session of DHC2-8 measurements from Bajnai et al. (2020). However, note that the corresponding raw data of Bajnai et al. (2020) was processed slightly differently for this study (see Methods).
Sample DVH-2 was prepared from the top ~300 μm of the outer surface of another slab of DHC2-8. The collection protocol is identical to that described by Daëron et al. (2019) for DVH-1, a previously collected subsample from the same slab surface.

(2) Laghetto Basso calcite, sample LGB-2
Laghetto Basso is a small 0.5 m deep lake in Corchia Cave, Italy. Sample LGB-2 represents subaqueous calcite that precipitated at the bottom of the lake. The lake has a modern stable temperature of 7.9 $\pm$ 0.2 °C. Based on the long residence-times of water in the cave and the lake, respectively, a low calcite saturation index of < 0.3, slow Holocene precipitation rates (0.3 μm/yr) and consistent $\delta^{18}O$ values for contemporaneously deposited calcite layers it has been argued that Laghetto Basso calcite precipitated very close to equilibrium (Daëron et al., 2019).

Table 1

Formation temperatures, number of replicates (n), average oxygen and dual clumped isotopic compositions (with associated 2 SE) of calibration samples and technical calcite GU 1. Oxygen isotope data are reported relative to VSMOW, considering an acid fractionation factor of 1.0081 at 90 °C (Kim et al., 2007).

Sample	T (°C)	Analytical session	n	$\delta^{18}O$ (‰)	Δ_{47}-I-CDES 90 (‰)	Δ_{47}-CDES 90 (‰)	2 SE (‰)	Δ_{48}-CDES 90 (‰)	2 SE (‰)
Laghetto Basso LGB-2	7.9 ± 0.2	28.07.-27.08.2020	9	26.63	0.667	0.651	0.006	0.260	0.023
Devil's Hole DVH-2	33.7 ± 0.2	28.07.-27.08.2020	9	14.77	0.582	0.569	0.006	0.246	0.023
Devil's Hole DHC2-8	33.7 ± 0.2	28.07.-27.08.2020	8	14.72	0.585	0.573	0.006	0.234	0.025
Devil's Hole DHC2-8	33.7 ± 0.2	02.09.-25.11.2019	9	14.69	0.572	0.568	0.006	0.234	0.023
Devil's Hole DHC2-8	33.7 ± 0.2	02.05.-05.08.2019	5	14.65	0.576	0.568	0.008	0.247	0.031
DHC2-8 total			*22*		*0.578*	*0.570*	*0.004*	*0.237*	*0.015*
CA 120*	120 ± 2	11.06.-15.07.2020	4	2.45	0.403	0.397	0.009	0.174	0.035
CA 170*	170 ± 2	11.06.-15.07.2020	5	−1.10	0.344	0.340	0.008	0.168	0.031
CA 200*	200 ± 2	11.06.-15.07.2020	6	−3.44	0.325	0.322	0.007	0.171	0.029
CA 250A*	250 ± 2	11.06.-15.07.2020	5	−5.51	0.295	0.292	0.008	0.148	0.031
CA 250B*	250 ± 2	11.06.-15.07.2020	6	−4.08	0.295	0.293	0.007	0.141	0.029
CM 351	727 ± 10	11.06.-15.07.2020	7	28.82	0.195	0.194	0.007	0.122	0.026
CM 351	727 ± 10	24.03.-05.06.2020	10	28.84	0.206	0.205	0.006	0.118	0.022
CM 351 total			*17*		*0.201*	*0.201*	*0.004*	*0.120*	*0.017*
ETH 1–1100	1100 ± 10	24.06.-28.07.2020	10	28.43	0.179	0.179	0.006	0.118	0.022
ETH 2–1100	1100 ± 10	24.06.-28.07.2020	10	11.89	0.184	0.184	0.006	0.123	0.022
GU 1		24.06.-28.07.2019	12	4.69	0.226	0.226	0.005	−0.413	0.020
GU 1		28.07.-27.08.2019	8	4.77	0.226	0.226	0.006	−0.427	0.025
GU 1 total			*20*		*0.226*	*0.226*	*0.004*	*−0.419*	*0.016*

*Residual sample aliquots from the calibration of Jautzy et al. (2020).

LGB-2 was collected from the top of core CD 3–12, a few centimeters away from core CD 3, which has been described by Drysdale et al. (2012). The collection protocol is identical to that described by Daëron et al. (2019) for LGB-1, a previously collected sub-sample from the same core surface.

(3) Hydrothermal calcites CA 120, CA 170, CA 200, CA 250A, CA 250B

Precipitation of hydrothermal calcites was performed using high pressure and temperature reaction cells at temperatures of 120 °C, 170 °C, 200 °C and 250 °C. Temperature was controlled within ±2 °C. Solutions of $NaHCO_3$ and $CaCl_2$ were isotopically equilibrated separately at the target temperature and under sufficient N_2 pressure to avoid fluid ebullition and potential vapour/fluid isotopic fractionations for at least 24 h. The longer than usual isotopic equilibration time at these temperatures takes into account recent work (Guo, 2020) that showed that in the CO_2-H_2O-DIC system, clumped isotopic equilibration is sluggish relative to that of singly substituted isotopologues. Once equilibrated, the two solutions were carefully mixed at high pressure and at saturation index below 2.1 ensuring relatively slow precipitation rate over a 24 h period. The reactors were then rapidly cooled down in a water/ice bath (<45 min) prior to depressurization to avoid retrograde clumped isotopic reordering or potential disequilibrium precipitation during fast degassing at high temperature. Precipitates were then further filtered and air-dried prior to storage in a desiccator until analysis. Calcite mineralogy was tested and confirmed by XRD analyses on each precipitate. Samples analysed in this study (CA 120, CA 170, CA 200, CA 250A and CA 250B) represent the residual aliquots of samples considered for the $\Delta_{47} - T$ calibration of Jautzy et al. (2020). Oxygen isotope analysis revealed that the produced calcites precipitated close to equilibrium. Full details can be found in Jautzy et al. (2020) and associated Supporting Information.

(4) High-temperature calcites CM 351, ETH 1-1100, ETH 2-1100

CM 351 is Carrara marble that was heated to 727 °C for 3 h at 170 MPa and afterwards quenched to room temperature. The sample experienced a strong γ-5 deformation supporting recrystallization at high temperature. Recrystallization was confirmed by microscopic inspection (Schmid and Bernasconi, 2010).

ETH 1-1100 and ETH 2-1100 are aliquots of ETH 1 and ETH 2 (Bernasconi et al., 2018), respectively, which were heated to 1100 °C at a pressure of 200 MPa for 24 h. Both equilibration experiments were done in Au_{90}-Pd_{10} capsules with a length of 40 mm and 4 mm outer diameter. The sample material was filled and compressed in the capsule and welded shut under an Ar stream using a Lampert PUK arc welder. Run A was filled with 0.54863 g of fine ground ETH 1 standard material of which 0.54514 g were recovered. Run B had 0.56816 g of fine ground ETH 2 standard material

with 0.56040 g recovered. Neither of the experiments displayed a weight difference after the experimental run. Experimental runs Run A and Run B were performed in externally heated pressure vessels (EHPV or "cold-seal" apparatus) at the Institute of Geochemistry and Petrology, ETH Zürich. Argon is utilized as pressure medium. At run conditions the hot end of the EHPV is in a sub-horizontal position of +10° inclination (hot-end up), which prevents circulation of the gas. The capsules were loaded directly into the hot-end of the vessel and heated to final temperature within six hours. Prior to heating, the pressure was set to 1000 bar at room temperature. At final run temperature (1100 °C), pressure was adjusted from ~1860 bar to final run conditions (2000 bar) and held there for 24 h. The temperature gradient within the (extended) hot zone of the vessel was ±10 °C and the accuracy of the temperature measurement is better than 10 °C. Pressure conditions were stable within 10 bars for the entire run duration. Quenching is accomplished via rotating the entire furnace and vessel to a 90° vertical position. The capsule drops to the cold-end and is quenched to room temperature within seconds. After successful quenching, the vessel was un-mounted and the capsule recovered. The capsule was then carefully opened with a razor blade and the slightly compacted material was recovered and fine ground in an agate mortar.

In addition to these 11 calcite samples, we analysed the dual clumped isotopic composition of a variety of inorganic carbonates (geothermal pipe carbonates, experimental precipitate MD 1; Table 2) of known precipitation temperatures to test the robustness of our $\Delta_{47} - \Delta_{48}$-T relationships. These inorganic carbonates are ideal for this purpose since their formation conditions imply relatively rapid isotopic equilibration rates (Section 5.4.1). We also reprocessed sample data from Bajnai et al. (2020) according to the outline provided in Section 3.3.

(5) Low-temperature carbonate MD 1

The low-temperature precipitate MD 1 was synthesized using an adapted CO_2-diffusion technique (Dietzel et al., 2004; Niedermayr et al., 2013). Initially, a 10 mM $CaCl_2$ solution (5 L) was prepared in an acrylic glass vessel, which was placed in a temperature-controlled water bath at 25.0 ± 0.5 °C. The solution was stirred at 150 rpm with a floating magnetic stirring bar. The pH of this outer solution was kept constant at pH 8.30 ± 0.03 by automatic titration of a 0.5 M NaOH solution using a Schott TitroLine alpha plus titrator. At the start of the experiment, a polyethylene bag containing 0.5 L of a freshly prepared 0.83 M $NaHCO_3$ solution (stirred for 30 min at pH 7.92 ± 0.02) was placed into the Ca^{2+} bearing outer solution. Ultrapure water (Millipore Integral 3: 18.2 $M\Omega cm^{-1}$) and analytical grade chemicals ($CaCl_2 \cdot 2H_2O$ and $NaHCO_3$ from Roth) were used for preparation of the solutions. Due to the CO_2 partial pressure gradient between the inner ($Pco_2 = 10^{-0.20}$ atm) and outer solution ($Pco_2 = 0$ to $10^{-3.92}$ atm from the initial to final solution, respectively), gaseous CO_2

Table 2
Geothermal pipe carbonates and experimental precipitate MD 1: Growth temperature, pH, growth rates, oxygen isotopic composition of parent water and carbonate (relative to VSMOW), as well as dual clumped isotopic compositions (CDES 90), associated 2 SE uncertainties, number of replicates (n) analyzed per sample and apparent and experimental equilibrium oxygen isotope fractionations.

Sample	Analytical session	T (°C)	pH	growth rate	δ^{18}O-H$_2$O (‰)	δ^{18}O-CaCO$_3$ (‰)	Δ_{47}-CDES 90 (‰)	2 SE (‰)	Δ_{48}-CDES 90 (‰)	2 SE (‰)	n	1000ln$a$(CaCO$_3$-H$_2$O)$_{app.}$ (‰)	1000ln$a$(CaCO$_3$-H$_2$O)$_{equ.}$ (‰)
BUK 1	27.07.-06.09.2020	53 ± 3	6.6	4 mm/yr	−11.1	13.7	0.521	0.007	0.203	0.026	7	24.8	23.2 (±0.4)*
BUK 2	27.07.-06.09.2020	45 ± 3	6.6	up to 50 mm/yr	−11.1	13.7	0.518	0.007	0.215	0.026	7	24.8	24.6 (±0.5)*
FAS 2	27.07.-06.09.2020	92 ± 3	7.5	n.a.	−12.0	6.2	0.437	0.007	0.193	0.026	7	18.3	18.0 (±0.4)*
KAK 1	27.07.-06.09.2020	100 ± 3	7.4	50 mm/yr	−10.3	8.1	0.438	0.007	0.200	0.026	7	18.4	17.1 (±0.3)*
SZE 3	27.07.-06.09.2020	96 ± 2	n.a.	3 mm/yr	−11.5	6.2	0.434	0.007	0.171	0.026	7	17.7	17.5 (±0.2)*
MD 1	05.04.-05.08.2019	25 ± 0.5	7.9–8.3	1.96 μmol h^{-1}l^{-1}	−9.3	18.9	0.598	0.005	0.254	0.021	11	28.1	28.2 (± 0.1)[#]

*Calculated after Friedman and O'Neil (1977), modified from O'Neil et al. (1969): 1000lnα(CaCO$_3$-H$_2$O) = 2.78 10^6/T^2 – 2.89; # calculated after Bajnai et al. (2018), modified from Kim and O'Neil (1997): 1000lnα(CaCO$_3$-H$_2$O) = 18030/T – 32.23.

diffuses through the polyethylene membrane (0.2 mm thickness) from the inner $NaHCO_3$ solution into the outer Ca^{2+} bearing solution. Accordingly, dissolved inorganic carbon (DIC) accumulates in the outer solution until a saturation index with respect to calcite ($SI_{calcite}$) of about 1 is reached, which initiates $CaCO_3$ precipitation (at about 8 h of experimental time). After the total experimental run time of 20 h, the precipitate was separated from the outer solution using a suction filtration unit equipped with a 0.2 μm cellulose acetate filter. The separated precipitate was rinsed with ultrapure water, dried at 40 °C and subsequently prepared for solid phase characterization. XRD results indicate that the precipitate consists of calcite (43 wt%) and vaterite (57 wt%). The fraction of the individual $CaCO_3$ polymorphs was quantified by using distinct peak areas from XRD pattern according to the relations reported in Niedermayr et al. (2013). The calcite crystals with sizes between 10 and 20 μm exhibit typical rhombohedral shape, while the vaterite crystals display roughly hexagonal plates between 3 and 15 μm.

(6) Geothermal pipe carbonates BUK 1, BUK 2, FAS 2, KAK 1, SZE 3

"Scaling" refers to the unwanted process of fluid-solid interaction resulting in variable mineral deposition from (thermal) waters of typically elevated mineralization (and often increased gas contents). It can result in a problematic reduction of water flow in technical circuits and drainages and blockage of technical components (e.g. pipes, valves, pumps, filters, heat exchangers) and, hence, in reduced working fluid and energy transfers (e.g. geothermal energy production, oil/gas exploitation, gas storage facilities, tunneling and mining).

The scale deposits used in this study – referred to as "geothermal pipe carbonates" – were recovered from thermal water transport pipelines made of conventional steel or plastics (PE) close to the wellhead (uppermost part of a borehole) of deep geothermal wells in Hungary (Pannonian Basin sedimentary aquifers). The geothermal facilities are used for district heating (communal buildings), heating of greenhouses (agriculture) and balneological applications (wellness, health resorts). The mineral deposits were recovered from pipe sections before major and intended outgassing of CO_2, steam and other gases in gas separators occurs.

The geothermal pipe precipitates dominantly consist of Ca-carbonate – either calcite (also Mg-calcite) or aragonite – with minor contributions of other precipitates or detrital components (amorphous silica, quartz, Fe-minerals, heavy metal sulfides, sulfates). The sample powders analyzed in this study were extracted from selected (pure) sample subsections and the individual samples crystallized under relatively constant physicochemical conditions (water-temperature, pressure, hydrochemistry, flow rate). Considering the environmental conditions of the different scale deposits investigated here, they represent a broad range of

hydrochemical compositions (speciation, pH), borehole depth (1000–2500 m), water flow rate (~20–75 m^3/h) and operating pressure (~0,5–10 bar at the wellhead). Further, they have crystallized within a broad fluid-temperature range of 45–100 °C at relatively constant temperature ($\pm 2 - 3$ °C), i.e. constant thermal water and geothermal energy production conditions are typically targeted in the technical facilities.

Geothermal pipe carbonate samples BUK 1 and BUK 2 consist of (low Mg) calcite and originate from a pipeline tapping a 1000 m deep well in a Devonian dolomite aquifer providing a water discharge of ~43 m^3/h for a geothermal facility (balneology) in Bükfürdo (NW-Hungary). The overall 36 mm thick sample BUK 1 formed at 53 $\pm$ 3 °C with some distance from the wellhead and the 7 mm thick sample BUK 2 precipitated close to a water outlet at 45 $\pm$ 3 °C. FAS 2, made of Mg-calcite, was recovered from a horizontal pipeline in Fábiánsebestyén (SE-Hungary) only a few meters from the wellhead of a 2012 m deep well connected to the regional Upper Pannonian aquifer (sandstone, marl) producing a water discharge of ~45 m^3/h. The overall 48 mm thick sample precipitated at 92 $\pm$ 3 °C. KAK 1 from Kakasszék (SE-Hungary) consists of Mg-calcite and was deposited in a horizontal steel pipe near the wellhead (~3 m) of a ~2000 m deep well discharging ~30 m^3/h of thermal water from the Upper Pannonian aquifer. The borehole is characterized by some pulsating water flow (high natural gas content) and water discharge is artesian. The overall 52 mm thick pipe carbonate formed at 100 $\pm$ 3 °C. Scale sample SZE 3 from Szentes (SE-Hungary) made of Mg-calcite was recovered near the wellhead (~4 m) of a 2400 m deep well discharging thermal water at a relatively constant rate of ~75 m^3/h from the widespread Upper Pannonian aquifer (sandstone, marl). The 9 mm thick sample crystallized at 96 $\pm$ 2 °C. Precipitation temperature, pH and $\delta^{18}O$ of the parent fluid, as well as growth rates of the geothermal pipe carbonates and MD 1, are compiled in Table 2.

(7) Other samples

Additional samples considered for a comparison with the $\Delta_{47} - \Delta_{48}$ - T relationships determined in this study (valid in a temperature range from 7.9 to 1100 °C) include a speleothem-like sample (MHD-1), a belemnite (66–465), a brachiopod (Mv143b), a cold-water coral (JR) and a warm-water coral (PC1_2005) (Table 3). These samples have precipitation temperatures varying between 7.2 $\pm$ 1.0 °C and 30.7 $\pm$ 0.3 °C which are, within their uncertainty, at the low end of the applicable range of our $\Delta_{47} - \Delta_{48}$ - T relationships. Further information about these samples can be found in Bajnai et al. (2020).

These samples have already been analysed by Bajnai et al. (2020), but were processed before the I-CDES became available. We have, therefore, reprocessed the original data according to the protocol outlined in the Methods section.

Table 3
Samples reprocessed from Bajnai et al. (2020): temperatures of formation, dual clumped isotopic composition, associated 2 SE uncertainties and number of replicates (n) analyzed per sample.

Sample	Analytical session	type/species	T (°C)	Δ_{47}-CDES 90 (‰)	2 SE (‰)	Δ_{48}-CDES 90 (‰)	2 SE (‰)	n
MHD-1	02.05.-05.08.2019	synthetic speleothem	30.7 ± 0.3					6
				0.546	0.007	0.277	0.029	
PC1_2005	05.04.-05.08.2019	*Porites lutea*	29.3 ± 1.0					10
				0.617	0.006	0.139	0.022	
Mv143b	05.04.-05.08.2019	*Magellania venosa*	11.4 ± 1.7					9
				0.664	0.006	0.257	0.023	
JR	05.04.-05.08.2019	*Desmophyllum pertusum*	7.2 ± 1.0					10
				0.710	0.006	0.201	0.022	
66–465	05.04.-05.08.2019	*Belemnopsis sp.*						9
				0.601	0.006	0.255	0.023	

3. METHODS

3.1. Sample preparation

All samples were analyzed for their dual clumped isotopic composition using the automated analytical setup (HAL attached to a ThermoFisher Scientific 253plus) described in Fiebig et al. (2019). HAL follows arrangement of the same key design elements (low blank autosampler, cold traps, packed GC-column with backpurge, online equilibrated gas introduction with identical flow-path as samples) as originally described for the "Caltech" type line by Passey et al. (2010). Major modifications to this type include the use of electropolished stainless steel wherever possible and two turbo-pumps (each backed-up by a water-trap) which pump the parts before and behind the GC separately (Fiebig et al., 2019).

Aliquots of 9.6–10.2 mg per replicate were loaded into silver capsules and reacted with > 106 wt-% H_3PO_4. Acid digestion temperature was set to 90 °C. Sets of three CO_2 gases with distinct bulk isotopic compositions, either equilibrated at 25 °C or 1000 °C, as well as international carbonate reference materials ETH 1, ETH 2 and ETH 3 were regularly analyzed along with the samples in order to correct for non-linearity and scale compression. At least one set of CO_2 equilibrated at 25 °C and one set equilibrated at 1000 °C, were analyzed per week. Gases equilibrated at 1000 °C cover δ^{47} and δ^{48} ranges of $-25‰ < \delta^{47} < 20‰$ and $-20‰ < \delta^{48} < 30‰$, respectively, whereas gases equilibrated at 25 °C exhibit δ^{47} and δ^{48} ranges of $-30‰ < \delta^{47} < 45‰$ and $-10‰ < \delta^{48} < 90‰$, respectively. In addition, every third sample loaded to the low blank autosampler represented ETH 1, ETH 2 or ETH 3, such that a full set of ETH 1–3 was always measured interspersed between six samples. Equilibrated gases were prepared following the protocol of Fiebig et al. (2019). The gases were finally transferred into autofingers and connected to the equilibrated-gas-port of HAL. Within HAL, equilibrated gases and carbonate-derived CO_2 follow the same purification pathway, with the exception that equilibrated gases do not pass the phosphoric acid bath (Fiebig et al., 2019).

Weighted aliquots of carbonate samples and references were stored in a vacuum cabinet at 30 °C for at least one day prior to being loaded in the autosampler. The low blank autosampler with its 50 positions was only vented and loaded once or twice a week.

3.2. Mass spectrometric analysis

HAL automatically transfers the purified CO_2 to the sample bellow of the dual inlet system of the 253plus. With each new sample, the working gas bellow is filled with an amount of reference gas CO_2 that corresponds to the amount of sample (derived) CO_2 (ca. 100 μmol). Pressure of sample and working gas ($\delta^{13}C_{VPDB} = -4.20‰$, $\delta^{18}O_{VSMOW} = 25.26‰$) is adjusted to values corresponding to an intensity of 16000 ± 100 mV at m/z = 44. Each sample is measured in 13 acquisitions, consisting of 10 cycles each. Working and sample gas bellow are re-adjusted to reach 16000 ± 100 mV again between acquisitions. Integration time is set to 20 s, corresponding to a total integration time of 2600 s per replicate. With these conditions the shot noise limit is 23.4 ppm for Δ_{48} and 8.0 ppm for Δ_{47} (Merritt and Hayes, 1994). Samples were analyzed in 4 – 11 replicates.

3.3. Data processing

All data was processed with our own Python code (Pysotope) using IUPAC ^{17}O correction parameters as recommended by Daëron et al. (2016). Δ_{47} data is both reported on the Carbon Dioxide Equilibrium Scale (CDES 90, Dennis et al., 2011), i.e. normalized to CO_2 equilibrated at temperatures of 25 °C and 1000 °C and an acid reaction temperature of 90 °C (Petersen et al., 2019), and on the InterCarb-Carbon Dioxide Equilibrium Scale (I-CDES, Bernasconi et al., 2021), i.e. normalized to carbonate reference materials ETH 1, 2 and 3 (Section 3.3.1). Δ_{48} data is reported in the CDES 90 reference frame, anchored to equilibrated gas data and an acid digestion temperature of 90 °C (Section 3.3.2). The individual steps associated with I-CDES and CDES 90 data normalization are explained below. Flow charts illustrating the arrangement of the individual steps are provided in the Supplementary (I-CDES data normalization: Fig. S1; CDES 90 data normalization: Fig. S2).

3.3.1. Δ_{47} data evaluation

The 253plus is equipped with a half-mass cup at m/z 47.5 which allows continuous monitoring of the negative

background on the m/z 47 and m/z 48 collectors. Negative background levels proportional to the m/z 47.5 signal can then be added to the measured intensities of m/z 47, m/z 48 and m/z 49 using scaling factors (Fiebig et al., 2019). Because the negative background is not the same below m/z 47, m/z 48 and m/z 49, scaling factors specific for each cup need to be determined in a given analytical session to achieve a proper background correction based on the measured m/z 47.5 intensity. For m/z 47 the proper factor is defined as that resulting in an average difference in absolute raw Δ_{47} of -3.3 ppm between ETH 1 and ETH 2 (Bernasconi et al., 2021). Strictly, this difference is valid on the I-CDES and not on the raw scale (vs working gas). With our 253plus, however, I-CDES and CDES scale compressions do not exceed 5 % (ETF slope value < 1.05) (Supplementary Material Sessions: Data). As a consequence, the bias in absolute Δ_{47} introduced this way is less than 0.2 ppm which is far below analytical precision. Within a given analytical session, equilibrated gases were background-corrected using the same m/z 47 scaling factor as that characteristic of ETH 1, 2. Notably, slopes characteristic of background corrected gas data were within errors almost always indistinguishable from zero in δ^{47} vs Δ_{47} space (Supplementary Material Sessions: Figures).

In a next step, transfer functions were determined to project background corrected raw Δ_{47} values to the I-CDES and the CDES 90. In order to constrain the session specific ETF's for the I-CDES, the means of background corrected raw Δ_{47} values were determined for ETH 1, ETH 2 and ETH 3 and correlated with the corresponding nominal Δ_{47} values reported by Bernasconi et al. (2021). In order to project background corrected raw Δ_{47} data to the CDES 90, intercepts displayed by equilibrated gases in δ^{47} vs Δ_{47} space were correlated with accepted Δ_{47} values of 0.9196‰ and 0.0266‰ for CO_2 equilibrated at 25 °C and 1000 °C, respectively (Petersen et al., 2019).

After projecting raw Δ_{47} values to the CDES 90 and I-CDES, residuals of each replicate from its long-term sample mean value can be plotted as a function of time. This is shown for the residuals in Δ_{47} (CDES 90) in Fig. 1a. It becomes obvious that small, slow, but systematic drifts occurred through time. These can either be attributed to subtle variations in the isotopic composition of the working gas and/or to small variations in acid reaction kinetics (e.g., Passey et al., 2010). In a final step, we therefore correct Δ_{47} (I-CDES) and Δ_{47} (CDES 90) values for this temporal drift. For this purpose, we determined for each session the offsets of measured ETH 1, ETH 2 and ETH 3 replicates relative to their nominal values by subtracting the nominal I-CDES (or CDES 90) value from the I-CDES (or CDES 90) values characteristic of the measured replicate. These offsets were plotted as a function of relative time. Relative time values (in days) were constrained based on the exact time when the first acquisition of a given replicate was started relative to the exact time when the session was started. Fourth order polynomial fits relating offsets to relative time values were used to calculate the offset specific for a given sample replicate, based on the relative time characteristic for the first acquisition of the replicate (Supplementary Material Sessions: Data

and Figures). For drift correction of Δ_{47} (CDES 90) values, ETH 3 was not considered to derive the session-specific fourth order polynomial expressions. The reason is that ETH 3 analyzed in this study exhibits a significant temporal drift in Δ_{47} that is not equally expressed by ETH 1 and 2, whose Δ_{47} (CDES 90) values were reproduced within errors between (sub)sessions (see Sections 5.1 and Fig. 2).

3.3.2. Δ_{48} and Δ_{49} data evaluation

For Δ_{48} and Δ_{49} it is still unknown if there are any significant differences between ETH 1 and ETH 2. In addition, for Δ_{48}, ETH 1, ETH 2 and ETH 3 are not suitable to create a transfer function since the repeatability of 36 ppm (Fig. 1b) is rather large relative to the ~160 ppm difference in Δ_{48} (CDES 90) between ETH 1/2 and ETH 3 (Bajnai et al., 2020). Furthermore, there are no internationally agreed Δ_{48} (I-CDES) values for these standards yet. Δ_{48} values are, therefore, reported on the CDES 90. For Δ_{49}, only background corrected raw values are reported (Supplementary Material Sessions: Data).

Proper scaling factors for background correction of m/z 48 and m/z 49 intensities based on measured m/z 47.5 intensities were determined for each analytical session using CO_2 equilibrated at 1000 °C and 25 °C, respectively, according to the assumption that equilibrated gas slopes in δ^{48} vs Δ_{48} and δ^{49} vs Δ_{49} space should be indistinguishable from zero (Supplementary Material Sessions: Data and Figures). Background corrected raw Δ_{48} values were finally projected to the CDES 90 based on theoretically expected values for CO_2 equilibrated at 25 °C ($\Delta_{48} = 0.345‰$) and 1000 °C ($\Delta_{48} = 0$) (Wang et al., 2004; Fiebig et al., 2019) and intercepts characteristic of 25 °C-CO_2 and 1000 °C-CO_2 sets of gases in δ^{48} vs Δ_{48} space. No drift correction was applied to Δ_{48} (CDES 90) values since no such systematic temporal variations were resolved in Δ_{48} residuals (Fig. 1b).

3.3.3. Analytical sessions

All samples were analyzed in five different sessions between April 2019 and September 2020 (Fig. 1a; Tables 1, 2, 3). Within session 5 we observed that the scaling factor for m/z 48 baseline correction (i.e., the factor that scales m/z 47.5 intensity to the negative background being effective below m/z 48) significantly drifted to lower values through time. This drift was caused by the ageing filament which finally failed in October 2020. In order to minimize potential biases introduced by this drift, we subdivided session 5 into different sample-specific sub-sessions (Table 1). Each of these sub-sessions spanned 4–6 weeks and has its own specific scaling factors for m/z 47, m/z 48 and m/z 49 background corrections (see Supplementary Material Sessions: Data). These intervals were arranged according to the time necessary to run the specific replicates of a given sample. Replicates of a given sample were evenly distributed across these subintervals.

4. RESULTS

Mean Δ_{47} (I-CDES), Δ_{47} (CDES 90), Δ_{48} (CDES 90), $\delta^{13}C_{VPDB}$ and $\delta^{18}O_{VSMOW}$ of the calibration samples are

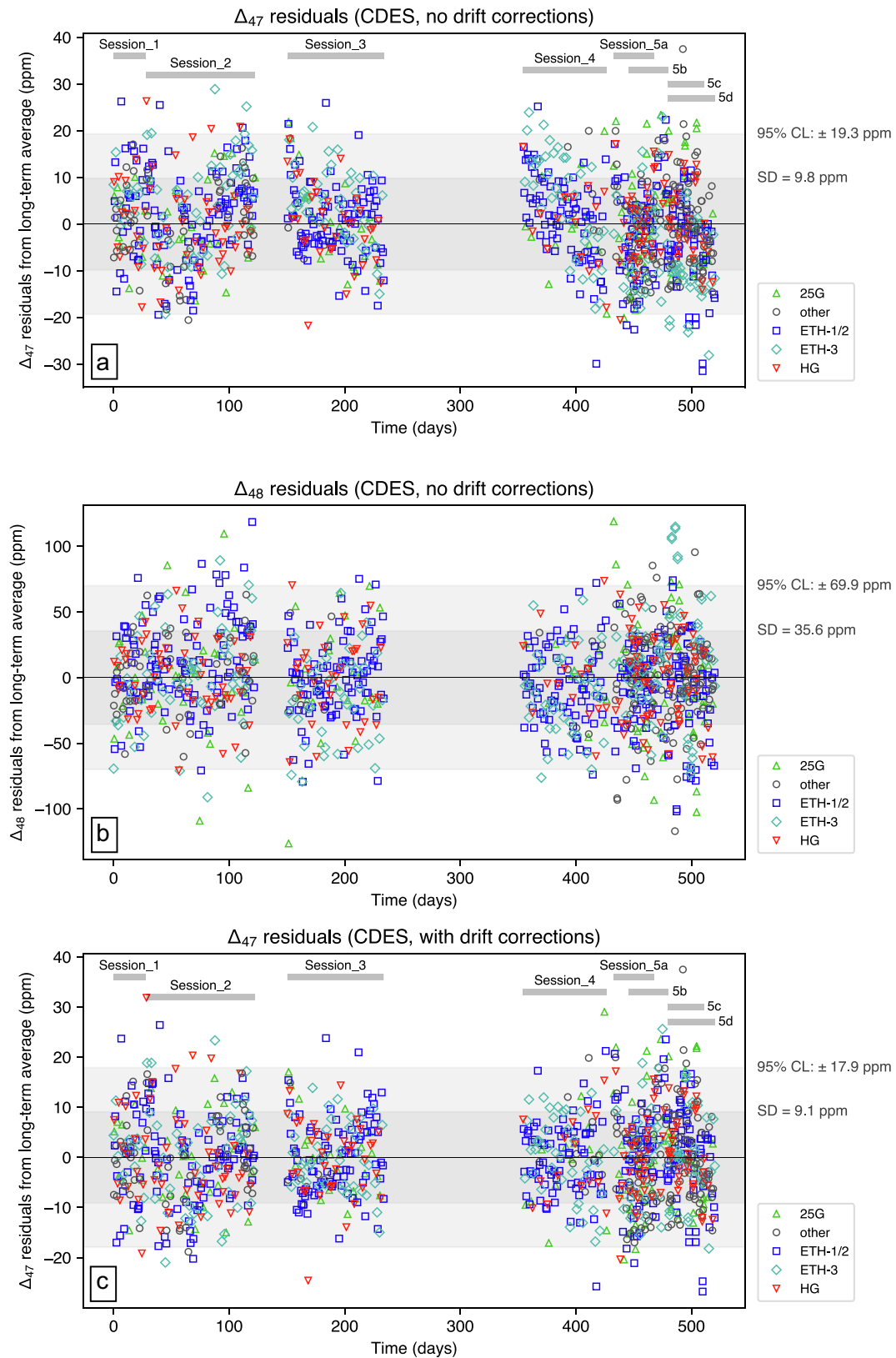Fig. 1. Plots of $\varDelta_{47}$ and $\varDelta_{48}$ residuals over time. (a) Residuals of non-drift corrected replicate $\varDelta_{47}$ (CDES 90) values from sample mean values. (b) Residuals of non-drift corrected replicate $\varDelta_{48}$ (CDES 90) values from sample mean values. (c) Residuals of drift corrected replicate $\varDelta_{47}$ (CDES 90) values from sample mean values.
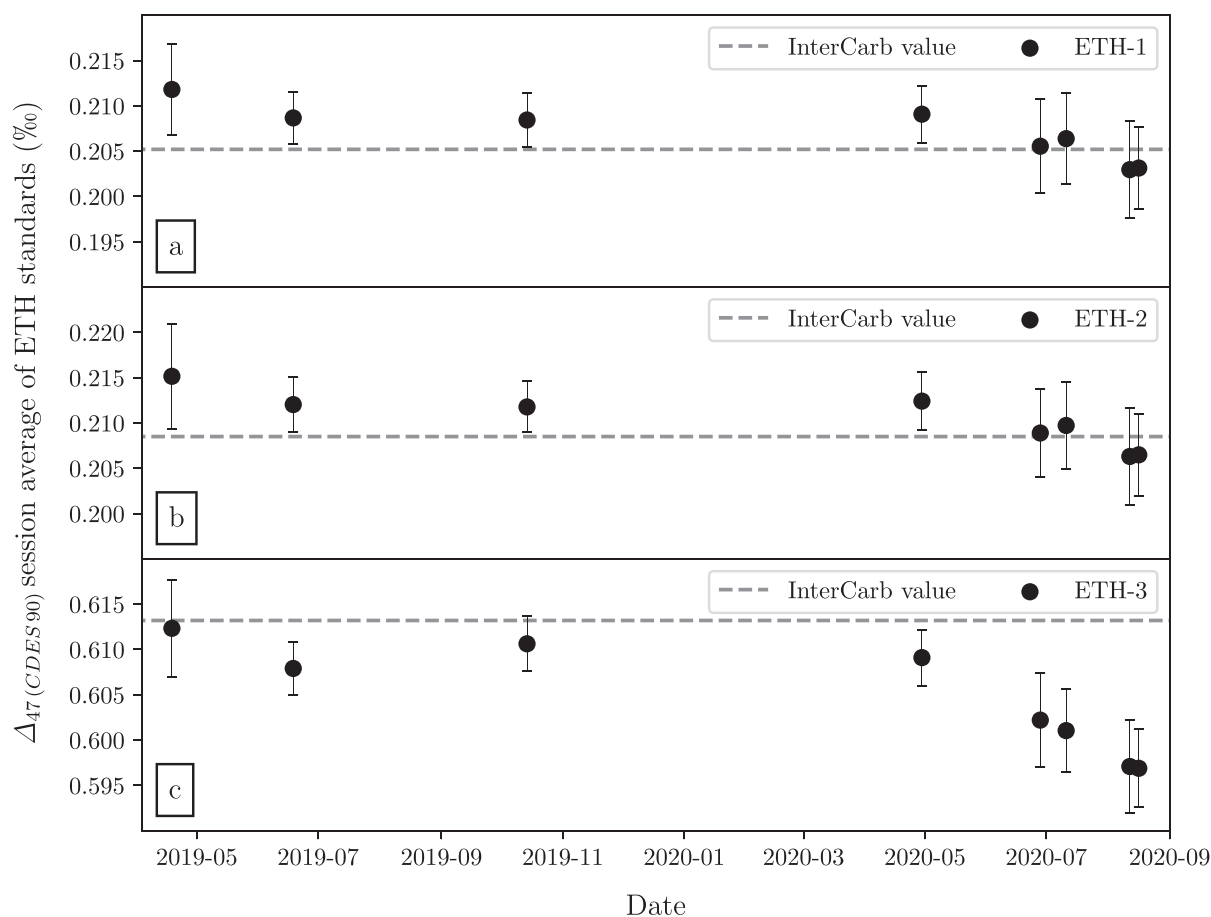
Fig. 2. Non-drift corrected session average Δ_{47} (CDES 90) values of ETH 1 (a), ETH 2 (b) and ETH 3 (c) through time. ETH 3 (c) displays a drift to Δ_{47} (CDES 90) values that are significantly smaller than the corresponding nominal InterCarb value. ETH 1 (a) and ETH 2 (b) also appear to show a drift to slightly lower Δ_{47} (CDES 90) values. However, in contrast to ETH 3, their session-specific mean values remain indistinguishable from each other within error and quasi-indistinguishable from their nominal InterCarb values. The apparent drift for ETH 1 and ETH 2 is, therefore, below our current analytical resolution.

shown in Table 1. The average dual clumped and bulk stable isotopic compositions of geothermal pipe carbonates and MD 1 as well as of the samples reprocessed from Bajnai et al. (2020) are provided in Table 2 and Table 3, respectively. Replicate raw data characteristic for a given analytical session is listed in the session-specific Supplementary Tables (Supplementary Material Sessions: Data).

Note that the listed Δ_{47}-values include drift correction, i.e. when the residual of each replicate from its corresponding sample mean value is plotted against time, drift is no longer apparent (Fig. 1c). The long-term 95% confidence limits for each replicate analysis are ±18 ppm for Δ_{47} (CDES 90) (Fig. 1c) and Δ_{47} (I-CDES 90), and ± 70ppm for Δ_{48} (CDES 90) (Fig. 1b). These estimates of analytical repeatability are based on a large number of pooled observations (1042 degrees of freedom, corresponding to a Student's t-factor value of 1.96). By contrast, sample-specific estimates of analytical repeatabilities, with degrees of freedom ≤ 10, are much less robust, as highlighted in several previous studies (e.g., Bonifacie et al., 2017; Fernandez

et al., 2017; Petersen et al., 2019; Daëron, 2021). The 95% confidence limits of the listed average Δ_{47} and Δ_{48} values are thus simply computed by dividing the long-term confidence limits reported above by the square root of the number of replicates considered.

5. DISCUSSION

Within each reference frame (I-CDES or CDES 90), different samples precipitated at identical temperatures (CA 250A, CA 250B), or heated to identical temperatures (ETH 1–1100, ETH 2–1100), exhibit negligible differences both in Δ_{47} and Δ_{48} values (Table 1), i.e. corresponding average values are within 2 SE from each other, as expected if clumped isotopic equilibrium is attained at a given temperature. Moreover, mean Δ_{47} and Δ_{48} values of the four different aliquots of Devils Hole section DHC2-8 (including DVH-2), which were analyzed in three different analytical sessions, all agree within 2 SE. The same applies to GU 1 analyzed in two different sessions (Table 1).

5.1. Comparison of Δ_{47} (I-CDES) with Δ_{47} (CDES 90) values

Δ_{47} (I-CDES) values of our 11 calibration samples are up to 16 ppm higher than the corresponding Δ_{47} (CDES 90) values. Most of these calibration samples were analyzed in session 5 for which it is observed that the positive difference between Δ_{47} (I-CDES) and Δ_{47} (CDES 90) increases linearly with Δ_{47} (Table 1). A paired Wilcoxon signed rank test reveals that the two data sets are distinguishable from each other at the 5% level (p = 0.0049). Relative to our equilibrated gas reference frame the Δ_{47} (I-CDES) frame, therefore, is slightly expanded. Notably, this positive difference remains of the same significance for the comparison between non-drift corrected Δ_{47} (I-CDES) and non-drift corrected Δ_{47} (CDES 90) (p = 0.042). As a consequence, the offset between Δ_{47} (I-CDES) and Δ_{47} (CDES 90) does not arise from the correction for drifts in the acid reaction environment.

Our large dataset (N = 1122), comprising 308 equilibrated gas analyses and 601 ETH standard analyses, offers an opportunity to assess how the CDES 90 and the I-CDES, which are nominally equivalent, compare with each other over a period of 500 days. Fig. 2 shows the session average Δ_{47} (CDES 90) values of ETH 1, ETH 2 and ETH 3, before any carbonate-based corrections, plotted as a function of time. Although the averages of ETH 1 and ETH 2 (Fig. 2a, b) remain indistinguishable from each other within error and quasi-indistinguishable from the corresponding nominal InterCarb value, there might be signs of a subtle decrease in ETH 1/2 values over time, on the order of only 8–9 ppm. By contrast, although ETH 3 averages agree within ± 5 ppm with the InterCarb value over the 400 first days, they decrease sharply after that, ending up significantly below the InterCarb value by 17 ± 5 ppm (2 SE) (Fig. 2c). The drift of ETH 3 to lower Δ_{47} (CDES 90) values occurred in session 5 when most of the calibration samples were analyzed.

Two simple explanations may account for the observation that – for a given sample analyzed within session 5 – Δ_{47} (I-CDES) values are significantly higher than corresponding Δ_{47} (CDES 90) values: (1) partial re-equilibration of carbonate-evolved CO_2 in the acid reaction vessel causing scale compression for the carbonate analyses while not affecting equilibrated gas standards (Swart et al., 2019), and (2) a compromised ETH 3 Δ_{47} composition as a result of slow dissolution-reprecipitation and/or oxygen exchange with water vapor over long periods. Isotopic alteration of ETH 3 would have become most effective in session 5 when the drift towards lower Δ_{47} (CDES 90) occurred (Fig. 2c). The first hypothesis can be safely ruled out. CO_2 equilibrated at a temperature of ≤ 90 °C is expected to have a Δ_{47} value $\geq 0.649‰$ (Petersen et al., 2019). Hence, re-equilibration at temperatures ≤ 90 °C would result in positive offsets for all three standards and greater offsets for ETH 1/2 than for ETH 3, very different from what is observed in Fig. 2a, b, c.

Adopting the second option as a working hypothesis, it does not make sense to compute I-CDES values in the usual way. However, we can still do so by treating ETH 1 and ETH 2 as I-CDES anchors, ETH 3 as an unknown sample whose composition is allowed to drift from session to session, and scale compression being constrained by the Δ_{47} difference between 25 °C and 1000 °C gases. This approach is conceptually equivalent to the CDES 90 correction outline with time-dependent carbonate corrections based only on ETH 1 and ETH 2 that we described in Section 3.3.1. The Δ_{47} (CDES 90) values obtained this way using Pysotope were independently confirmed processing our original raw data with the Δ_{47} crunch library (Daëron, 2021), using a pooled regression approach with ETH 1 and ETH 2 treated as anchors and constraining the average Δ_{47} difference between 25 °C and 1000 °C gases to be equal to 0.893‰ in all sessions (Δ_{47}-I-CDES[#] in Supplementary Table S1). The two approaches yield indistinguishable results well within analytical limits (Supplementary Table S1), as reflected by a paired Wilcoxon signed rank test (p = 0.48).

When we compare Δ_{47} (CDES 90) values of LGB 2 and DVH 2 made in session 5 to their previously published I-CDES values, measured independently at LSCE and anchored to the four ETH standards and no gas standards (Anderson et al., 2021), it becomes obvious that the GU and LSCE measurements are in excellent agreement, with $0.6508 \pm 0.0060‰$ vs $0.6486 \pm 0.0059‰$ (95 % CL) for LGB-2 and $0.5691 \pm 0.0060‰$ vs $0.5696 \pm 0.0054‰$ for DVH 2. These results independently confirm the validity of hypothesis (2) that the problem associated with the I-CDES normalization presented in this study is with ETH 3. We conclude that our Δ_{47} (CDES 90) values can be safely compared with I-CDES values obtained in other laboratories. Although the cause of the drift observed in ETH 3 remains unclear, our findings highlight the necessity to run at least one additional low-temperature standard (e.g., in-house carbonate or international standard such as IAEA-C2) along with carbonate samples and ETH standards to ensure prompt detection of compromised carbonate anchors.

5.2. Temperature dependence of Δ_{47} and Δ_{48}

Hill et al. (2014) determined the theoretical temperature dependences of multiple heavy isotope substitutions in calcite. The excess abundance of ^{13}C-^{18}O and ^{18}O-^{12}C-^{18}O bearing calcite isotopologues relative to a stochastic distribution of isotopes is expressed by Δ_{63} and Δ_{64} values, respectively. These differ from measured Δ_{47} and Δ_{48} values by the acid fractionation factors characteristic of acid digestion of m/z 63 and m/z 64 calcite isotopologues, respectively. The temperature dependences of theoretically computed Δ_{63} and Δ_{64} values are best expressed by fourth order polynomials of 1/T (Fig. 3a, b). In this case, both regression coefficients become 1, i.e. Δ-values predicted by these polynomials are identical to theoretically calculated Δ-values:

$$\Delta_{63}(‰) = -5.897 \; 1/T - 3.521 \; 10^3 1/T^2$$
$$+ 2.391 \; 10^7 1/T^3 - 3.541 \; 10^9 1/T^4 \tag{3}$$

$$\Delta_{64}(‰) = 6.002 \; 1/T - 1.299 \; 10^4 1/T^2$$
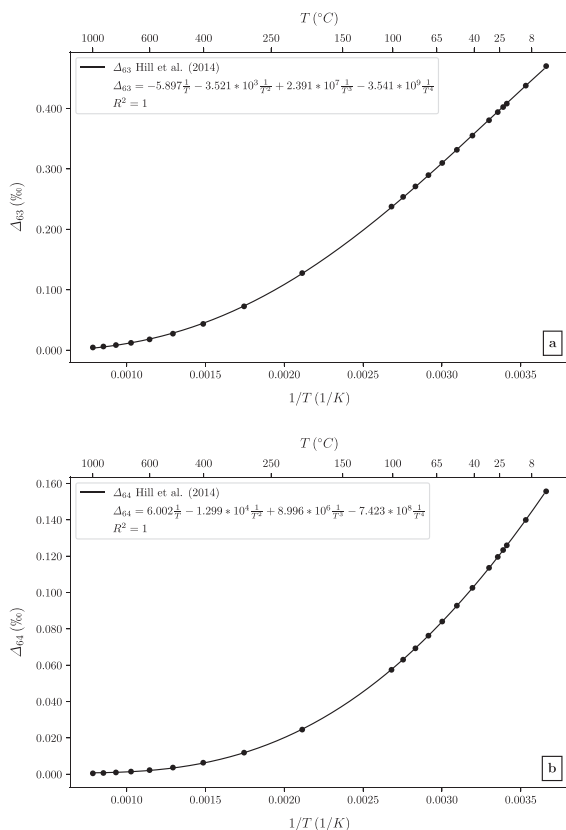$$+ 8.996 \; 10^6 1/T^3 - 7.423 \; 10^8 1/T^4 \tag{4}$$

Fig. 3. Temperature dependence of theoretically predicted carbonate Δ_{63} (a) and Δ_{64} (b) values after Hill et al. (2014). Corresponding regression coefficients R reach a value of 1 if fourth order polynomial relationships between Δ-values and $1/T$ are considered. This demonstrates that fourth order polynomials exactly describe the temperature dependence of theoretical Δ-values.

If Δ_{47}- and Δ_{48}-values characteristic of the calibration samples are plotted against $1/T$ it becomes obvious that measured data follow temperature trends that are very similar to those predicted for theoretical Δ_{63}- and Δ_{64}-values (Fig. 4a, b). In order to express the temperature dependence characteristic of our calibration samples, we, therefore, adjusted the theoretical curves to measured data adding scaling factors and a constant term to the theoretical expressions (3) and (4) (Fig. 4a, b). Both the scaling factor and the constant were determined using error-weighted least squares regressions. The following temperature relationships were obtained for Δ_{47} (CDES 90) and Δ_{48} (CDES 90):

$$\Delta_{47}(CDES\ 90)\ (\text{‰})\ =\ 1.038\Delta_{63}(\text{‰})\ +\ 0.1856 \qquad (5)$$

$$\Delta_{48}(CDES\ 90)\ (\text{‰})\ =\ 1.028\Delta_{64}(\text{‰})\ +\ 0.1245 \qquad (6)$$

Squared correlation coefficients (R^2) of 0.999 and 0.976 for Eqs. (5) and (6) respectively, provide evidence that the theoretical 4th order polynomials (Eqs. (3), (4)) excellently fit measured Δ_{47} and Δ_{48} values (Fig. 4a, b). The temperature sensitivities of Δ_{47} (CDES 90) and Δ_{48} (CDES 90) are slightly (i.e., ~ 3–4%) higher than predicted by theory. The constant terms of 0.1856‰ and 0.1245‰, respectively, represent the $\Delta_{47} - \Delta_{63}$ and $\Delta_{48} - \Delta_{64}$ acid fractionation factors at a digestion temperature of 90 °C. Fig. 4c finally

shows the calibration data in Δ_{47} (CDES 90) vs Δ_{48} (CDES 90) space, along with the Δ_{47} (CDES 90) and Δ_{48} (CDES 90) values predicted by Eqs. (5) and (6), respectively.

5.3. Comparison of Δ_{47} (CDES 90) calibration with previous Δ_{47} I-CDES calibrations

Two recent calibrations were predominantly made with extraction devices such as the Kiel IV and the NuCarb where only a few drops of phosphoric acid are added to an evacuated vial containing sub-mg aliquots of carbonate (Jautzy et al., 2020; Anderson et al., 2021). Anderson et al. (2021) reported their composite calibration data on the I-CDES, whereas Jautzy et al. (2020) expressed their Δ_{47} data against the ETH 1, 2 and 3 Δ_{47}-values recommended by Bernasconi et al. (2018). We reprocessed the original data of Jautzy et al. (2020) using the recently accepted Δ_{47} (I-CDES) values of Bernasconi et al. (2021). The calibration data set of Jautzy et al. (2020) (Supplementary Table S2) was finally enlarged by ETH 1–1100 and ETH 2–1100 Δ_{47} (I-CDES) data of Anderson et al. (2021) to extend their dataset to highest temperatures. Jautzy et al. (2020) and Anderson et al. (2021) originally used a third order $1/T$ polynomial and a linear $1/T^2$ regression line, respectively, to determine the temperature dependence of Δ_{47}. In order to compare the consistency of our data with these two calibrations, we fitted the theoretical 4th order polynomial of $1/T$ (Eq. (3)) the same way to their data as for ours. In its entire temperature range of 8–1100 °C, the largest offset between our CDES 90 calibration and these two calibrations is $\leq \pm 2$ ppm which is well in the 95% confidence limit of our calibration (Fig. 5a, b). Furthermore, reprocessed Δ_{47} (I-CDES) data of planktonic and benthic foraminifera (Peral et al., 2018) and of Laghetto Basso and Devils Hole calcite analyzed at LSCE (Anderson et al., 2021) is consistent with our Δ_{47} (CDES 90) calibration, i.e. plots in its 95% confidence band (Fig. 5c). These observations further support our earlier conclusion that our CDES 90 is equivalent to the I-CDES reference frame. Considering the nature of our samples and the consistency of our Δ_{47} (CDES 90) data with I-CDES calibration data from other labs we postulate that equation (5) and (6) describe good approximations of the temperature dependence of carbonate Δ_{47} and Δ_{48} equilibrium.

5.4. Robustness of the Δ_{47} (CDES 90) - Δ_{48} (CDES 90) - T relationships

We can now compare the Δ_{47} (CDES 90) and Δ_{48} (CDES 90) values of natural carbonates and experimental precipitates with the respective position of carbonate equilibrium to test the robustness of our calibration and to check for the significance of kinetic departures from equilibrium (Fig. 6a, b, c). Disequilibrium Δ_{47} and Δ_{48} values can be expected, if full reversibility is not attained within each single reaction step contributing to the reaction sequence of carbonate (bio)mineralization. In the CO_2-DIC-H_2O-$CaCO_3$ system, the most sluggish reactions are the hydration and hydroxylation of dissolved CO_2 to bicarbonate (Guo, 2020). Rapid degassing of CO_2 from an equi-
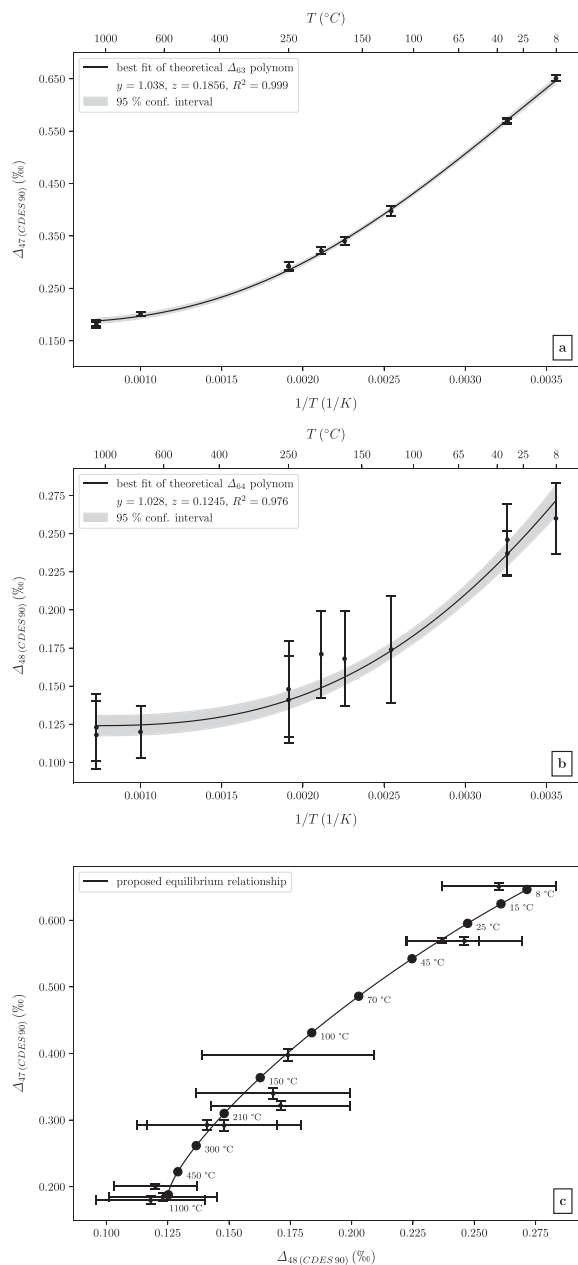
Fig. 4. Temperature dependence of Δ_{47}- and Δ_{48}- values as reflected by 11 calibration samples (Table 1). (a) Δ_{47} reported on the CDES 90; (b) Δ_{48} reported on the CDES 90. (c) Δ_{47} (CDES 90) vs Δ_{48} (CDES 90). All error bars correspond to 2 SE. (a, b) Theoretical fourth order polynomials obtained for Δ_{63} (Fig. 3a) and Δ_{64} (Fig. 3b) were adjusted to measured Δ_{47}- and Δ_{48}-values adding a constant term (z) and a scaling factor (y) to the respective equations. Adjustment of these parameters is based on error-weighted least square regression. The constant term z is equivalent to the Δ_{47}-Δ_{63} (a) and Δ_{48}-Δ_{64} acid fractionation factor (b) at a digestion temperature of 90 °C. Gray envelopes represent 95% confidence interval level. (c) For a given temperature, Δ_{47} (CDES 90) and Δ_{48} (CDES 90) values are predicted by Eqs. (5) and (6), respectively.

librated DIC solution and/or absorption of external CO_2 by an isotopically equilibrated DIC solution can lead to significant departures from homogeneous isotopic equilibrium

(Guo and Zhou, 2019; Guo, 2020). For example, if carbonate supersaturation is achieved through additional production of dissolved bicarbonate and carbonate ions from the absorption of external CO_2, departures above the equilibrium line upon precipitation are expected. In this case, isotopically disequilibrated DIC deriving from the hydration/hydroxylation reactions mixes with an equilibrated DIC fraction already present in the calcifying fluid prior to the onset of external CO_2 absorption (Guo, 2020). This process might be relevant for corals which initiate carbonate precipitation by pH up-regulation (e.g., Cohen and McConnaughey, 2003). On the contrary, supersaturation and precipitation can also be initiated by degassing of CO_2 from the calcifying fluid if the internal pCO_2 of the solution exceeds that of the surrounding environment. In this case, a kinetic isotopic CO_2 endmember deriving from the dehydration/dehydroxylation of dissolved bicarbonate is removed from the solution, leaving behind an isotopically-disequilibrated residual DIC fraction that is forced to re-equilibrate with the water again through the (de)hydration/(de)hydroxylation reactions. CO_2 degassing is expected to cause departures below the equilibrium line, and has been predicted to be important for some speleothems (Guo and Zhou, 2019). Earlier dual clumped isotope results agree well with theoretical expectations according to which isotopic disequilibrium signatures in coral skeletons and speleothems are introduced via CO_2 absorption and CO_2 degassing, respectively (Bajnai et al., 2020). Generally, equilibrium DIC-speciation and processes occurring at the solution-crystal interface could also contribute to isotopic disequilibrium in the overall $CaCO_3$-H_2O system (e.g., Zeebe, 1999; Watkins et al., 2014, Devriendt et al., 2017). The effect of interfacial kinetic isotope effects on the clumped isotopic composition of the precipitated carbonate, however, seems to be below current analytical resolution (e.g., Tang et al., 2014; Watkins and Hunt, 2015; Levitt et al., 2018). It has also been proposed that bond-reordering may occur at the crystal-solution interface such that clumped isotopic equilibrium is finally attained in the carbonate whereas heterogeneous oxygen isotopic equilibrium is not reached between $CaCO_3$ and H_2O (Tripati et al., 2015).

For the following comparison of measured samples with the position of $\Delta_{47} - \Delta_{48}$ equilibrium we considered that our Δ_{47} (CDES 90) - T (Eq. (5)) and Δ_{48} (CDES 90) - T relationships (Eq. (6)) have their own uncertainties as represented by their 95% confidence limits (Fig. 4a, 4b). The temperature-dependent 95 % uncertainties associated with these calibrations were determined based on known or inferred formation temperatures and propagated on the 2 SE characteristic of the sample considering that the overall uncertainty is represented by the square root of the square sum of the two individual uncertainties. All temperature uncertainties listed below are based on these propagated uncertainties.

5.4.1. Experimental precipitate MD 1 and geothermal pipe carbonates

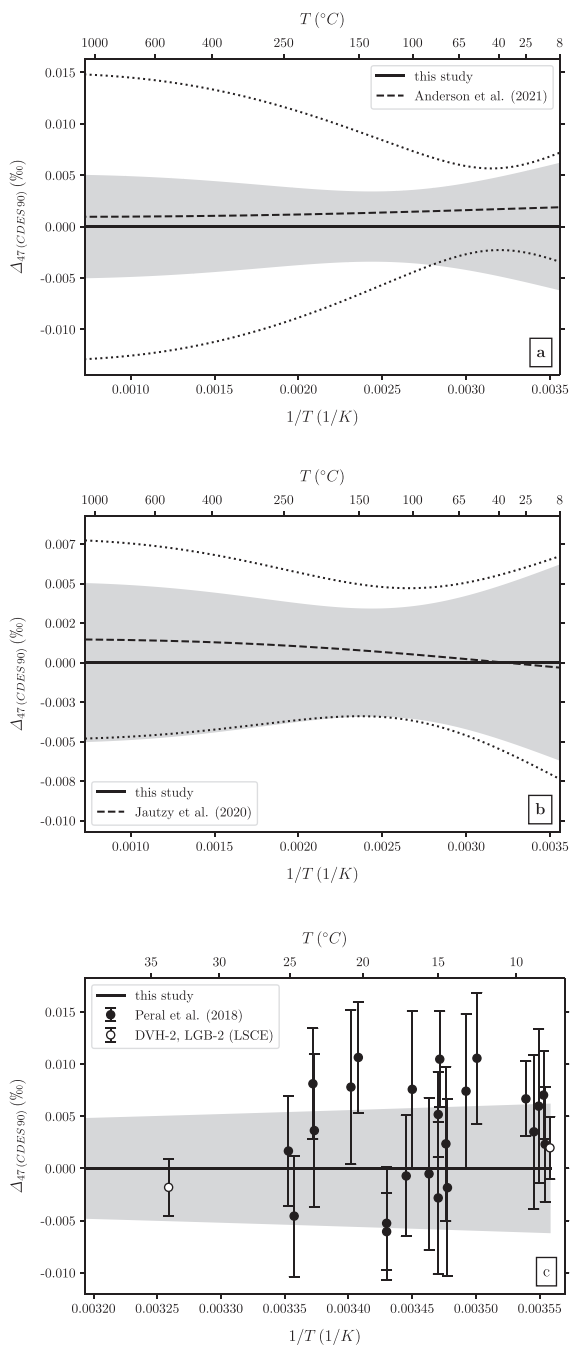Within errors, MD 1 plots on the equilibrium line (Fig. 6a, c). If projected to the equilibrium curve, its Δ_{47}

Fig. 5. Offsets of other Δ_{47} (I-CDES) calibrations/values from our Δ_{47} (CDES 90) calibration (Eq. (5)). (a) Offset Anderson et al. (2021); (b) offset Jautzy et al. (2020); (c) offsets LGB 2 and DVH 2 (Anderson et al., 2021) and reprocessed I-CDES data of Peral et al. (2018) on planktonic and benthic foraminifera. Data sets of Jautzy et al. (2020) and Anderson et al. (2021) were treated the same way as our data set, i.e. adjusting theoretical fourth-order polynomials (Eqs. (3) and (4)) to their data. Gray envelope around zero characterizes 95% confidence envelope of our calibration. Dashed lines in a) and b) represent average offsets of Jautzy et al. (2020) and Anderson et al. (2021) relative to our calibration and dotted lines the 95% confidence band of these offsets. Error bars in (c) correspond to 2 SE.

value indicates a temperature of $24.1^{+2.7}_{-2.7}$ °C which agrees with its original formation temperature of 25.0 ± 0.5 °C. The observed $1000\ln\alpha(CaCO_3\text{-}H_2O)$ of 28.1 is 1.6‰ lower than the equilibrium fractionation expected after Coplen (2007) and Daëron et al. (2019), but matches the 28.2 ± 0.1‰ expected for 25 °C according to the temperature dependence of the $CaCO_3\text{-}H_2O$ oxygen isotope fractionation factor of Kim and O'Neil (1997) (Table 2). It is reasonable to assume that the equation provided by Kim and O'Neil (1997) underestimates the true position of oxygen isotope equilibrium by ~1.5‰, independent of temperature (Coplen, 2007). Generally, carbonate-$\delta^{18}O$ values lower than those predicted by equilibrium point to the importance of kinetic effects occurring at the solution-crystal interface and/or within the solution (e.g., Devriendt et al., 2017). In the case of MD 1, the first crystals appeared 8 hours after the polyethylene bag containing the $NaHCO_3$ solution was placed in the $CaCl_2$ solution, and the dominant precipitation stage was reached after 13 hours. At a pH of ~8 and 25 °C, the dissolved carbon species require ~4 hours to reach oxygen and clumped isotope equilibrium once CO_2 absorption has been initiated (Guo, 2020). However, this temporal constraint does not consider that CO_2 absorption is limited by a diffusive flux of CO_2 across a membrane - as is the case in the setup chosen for MD 1 formation. It, therefore, remains unclear if the DIC pool attained full isotopic equilibrium prior to the onset of MD 1 precipitation. Irrespective of the origin of the kinetic oxygen isotope effect, recent studies concluded that no effect on Δ_{47} was resolvable in those calcites that were precipitated close to the oxygen isotope equilibrium limit, i.e. characterized by $\delta^{18}O$-values that are intermediate between those predicted by the equations of Kim and O'Neil (1997) and Coplen (2007) (Kelson et al., 2017; Levitt et al., 2018; Jautzy et al., 2020). Dual clumped isotope data on MD 1 appears to confirm these findings.

Geothermal pipe carbonate samples BUK 1, FAS 2, KAK 1 and SZE 3 plot within errors on the $\Delta_{47} - \Delta_{48}$-equilibrium line (Fig. 6a, b). Apparent Δ_{47}-derived equilibrium temperatures of $54.0^{+3.6}_{-3.6}$ °C, $96.2^{+4.7}_{-4.5}$ °C, $96.0^{+4.7}_{-4.6}$ °C and $98.0^{+4.9}_{-4.7}$ °C are consistent with measured water temperatures of 53 ± 3 °C, 92 ± 3 °C, 100 ± 3 °C and 96 ± 2 °C for BUK 1, FAS 2, KAK 1 and SZE 3, respectively. Sample BUK 2 also plots on the equilibrium line, reflecting an apparent Δ_{47}-derived equilibration temperature of $55.4^{+3.6}_{-3.6}$ °C. This temperature is higher than the 45 ± 3 °C measured at the vent of this site. BUK 1 and BUK 2 were sampled from the same pipeline system. While BUK 1 precipitated in the major thermal water transport pipeline, BUK 2 crystallized in a much smaller branch. Since both samples display identical temperatures that perfectly agree with the temperature of the fluid flowing through the major pipeline it seems possible that the temperature measured in the branched pipeline underestimates the fluid temperature having prevailed during growth of BUK 2. This assumption is supported by the notion that BUK 1 and BUK 2 exhibit identical $\delta^{18}O$ values (Table 2).

Close attainment of clumped isotope equilibrium in the investigated geothermal pipe carbonates is further consis-

tent with (i) kinetic constraints on isotope exchange in the CO_2-DIC-water system, (ii) the measured oxygen isotopic composition of these samples and (iii) previous observations on pipe carbonate $\varDelta_{47}$: (i) At ~50 °C and a pH of 6.6, i.e. the conditions specific for the formation of BUK 1 and 2, the DIC system is predicted to return to full isotopic equilibrium within < 5 minutes after CO_2 degassing has been initiated. This equilibration time reduces to ~1 minute at a temperature of ~95 °C and a pH of ~7.5, i.e. the conditions specific for the formation of FAS 2 and KAK 1 (Guo, 2020). (ii) The formation temperatures of the investigated pipe samples well exceed the range charac-

teristic of the calibration of Kim and O'Neil (1997) so that apparent oxygen isotope fractionations cannot be compared to those predicted by Kim and O'Neil (1997). However, the latter recognized that their calibration agrees perfectly with that of O'Neil et al. (1969) which is valid between 0–500 °C (note that the original temperature equation provided by O'Neil et al. (1969) needs to be slightly modified to account for a revised fractionation factor between CO_2 and H_2O of 1.0412 at 25 °C (Friedman and O'Neil, 1977)). Apparent $1000ln\alpha(CaCO_3-H_2O)$ values obtained for the pipe carbonates are 0.2 to 1.6‰ higher than predicted by Friedman and O'Neil (1977), independent of the precipitation temperature and the precipitation rate of the carbonate (Table 2). Provided the equilibrium oxygen isotope fractionation is ~1.5‰ bigger at any temperature than proposed by Friedman and O'Neil (1977), the observed positive offset of 0.2 to 1.6‰ relative to Friedman and O'Neil (1977) could correspond to the equilibrium limit, for which no effect on $\varDelta_{47}$ has been resolved. (iii) Kluge et al. (2018) previously interpreted the consistency between $\varDelta_{47}$-derived temperatures and measured fluid temperatures to be indicative for the attainment of clumped isotope equilibrium in geothermal pipe carbonates.

5.4.2. Reprocessed data for natural samples

Bajnai et al. (2020) analyzed the dual clumped isotopic composition of calcareous skeletons of a warm water coral (PC 1), a cold water coral (JR) and a brachiopod (MV-143b) grown at temperatures of 29.3 ± 1.0 °C, 7.2 ±
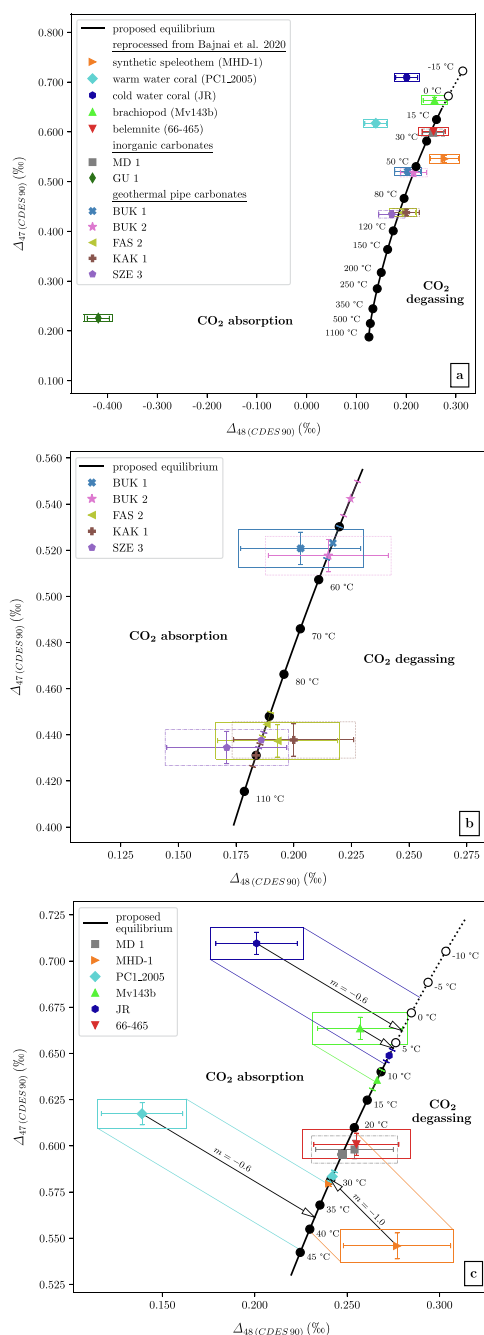

Fig. 6. Comparison of our proposed $\varDelta_{47} - \varDelta_{48}$-equilibrium relationship with dual clumped isotope data made on samples with independently known precipitation temperatures (except for the belemnite 66–465). All data is reported on the CDES 90. The dotted part of the equilibrium line (a) represents its extrapolation to temperatures < 8 °C. Kinetics associated with CO_2 absorption and CO_2 degassing reactions will cause departures above and below the equilibrium line, respectively (Guo, 2020). Sample mean values and their respective 2 SE are indicated by sample specific symbols and horizontal and vertical error bars of the same color (a, b, c). Symbols and vertical color-coded bars occurring on the equilibrium line (b, c) reflect independently known sample formation temperatures and their uncertainties. Color-coded boxes (a, b, c) represent propagated 2 SE uncertainties, considering both the 2 SE characteristic of a sample (Tables 1, 2, 3) and the 95 % confidence uncertainty of the calibration regression lines (Fig. 4a, b) specific for the temperature of sample formation. Boxes projected to the equilibrium line along theoretically predicted, process-specific linear kinetic trajectories (c) indicate the range of apparent sample formation temperatures devoid of a kinetic bias. (a) All sample data is displayed. Technical calcite GU 1 plots far off equilibrium. (b) Zoom-in of (a) showing geothermal pipe carbonate data. All pipe carbonates plot indistinguishable from equilibrium reflecting temperatures consistent with measured water temperatures. (c) Zoom-in of (a) displaying sample MD 1 and data reprocessed from Bajnai et al. (2020). Linear kinetic trajectories characteristic of the early stages of CO_2 absorption (slope −0.6) and CO_2 degassing (slope −1.0) are from Bajnai et al. (2020) (see also text and Fig. 7). With the exception of sample MD 1 and the belemnite (66–465), all samples exhibit disequilibrium $\varDelta_{47} - \varDelta_{48}$ patterns.

1.0 °C and 11.4 ± 1.7 °C, respectively. In addition, they analyzed calcite (MHD-1) precipitated under flowstone-like speleothem conditions at 30.7 ± 0.3 °C. At that time, they were only able to compare the Δ_{47} and Δ_{48} compositions of these samples to an earlier estimate of equilibrium, which was constrained by the theoretical temperature dependence of Δ_{63} and Δ_{64} and the dual clumped isotopic composition of Devils Hole carbonate DHC2-8. Their reprocessed data is shown in Fig. 6a, c along with our updated estimate of $\Delta_{47} - \Delta_{48}$ equilibrium. Like in the original study of Bajnai et al. (2020), the warm water and the cold water coral plot above the equilibrium line, whereas the speleothem-like sample plots below it. Within errors, the brachiopod plots indistinguishable from equilibrium. However, its Δ_{47} indicates a crystallization temperature which is significantly lower than the measured water temperature of 11.4 ± 1.7 °C. The extents to which these four samples depart from equilibrium are displayed in Fig. 7, along with modeled trajectories (loops) of carbonate Δ_{47} and Δ_{48} that can result from precipitation during CO_2 absorption or CO_2 degassing (for detailed info about model parameters see Bajnai et al., 2020). As already stated by Bajnai et al. (2020), the directions of departure from equilibrium conform with the hypothesis that the investigated marine organisms initiate carbonate precipitation through CO_2 absorption, whereas CO_2 degassing is the process dominating speleothem formation. The speleothem-like sample plots along the part of the loop that is characteristic of precipitation during the early stage of CO_2 degassing. This part of the loop can be approximated by a linear kinetic vector having a slope of −1. As suggested by Bajnai et al. (2020), this slope can, therefore, be taken to project the dual clumped isotopic composition of this sample onto the $\Delta_{47} - \Delta_{48}$ equilibrium curve to determine its kinetically unbiased formation temperature (Fig. 6c). Within their errors, the dual clumped isotopic compositions of the cold water coral aragonite and the brachiopod calcite still overlap with the linear vector of −0.6 that would be characteristic of kinetic effects introduced during the early stage of CO_2 absorption (Fig. 7). Therefore, the respective projected (with a slope of −0.6) formation temperatures devoid of the kinetic biases agree within errors with the measured water temperatures the cold water coral and the brachiopod lived in (Fig. 6c).

Different from the original study of Bajnai et al. (2020), the reprocessed dual clumped isotopic composition of warm-water coral PC 1 now plots significantly below the linear vector characteristic of early CO_2 absorption, i.e. in the curved region of the CO_2 absorption loop (Fig. 7). As a consequence, the unique slope of −0.6 cannot be applied anymore to correct for the kinetic bias in its dual clumped isotopic composition. Relative to its early, almost linear section, the curved part of the loop is indicative of carbonate precipitation during a more advanced stage of CO_2 absorption. Attainment of this advanced stage in the warm water coral is predicted by model simulations that consider the involvement of carbonic anhydrase (CA) in DIC equilibration. The hydration reaction speeds up with CA activity, reducing the extent of isotopic disequilibrium in the DIC

pool. Precipitation during an advanced stage of DIC equilibration has already been proposed to be relevant for warm water corals based on Δ_{47} and $\delta^{18}O$ data (Guo, 2020, see his Figure 9e).

Belemnite sample 66–465 was deposited during the Middle Oxfordian-Lower Tithonian at DSDP site 511 on the Falkland Plateau (51°00.28′S, 46°58.30′W) (Vickers et al., 2019). Our improved assessment of equilibrium confirms the original conclusion of Bajnai et al. (2020) that it likely precipitated in clumped isotope equilibrium. Its Δ_{47} (CDES 90) value indicates a temperature of $23.1^{+2.8}_{-2.8}$ °C (Fig. 6a, c), confirming the relatively warm temperatures that were proposed for the upper part of the water column for this Early Cretaceous, southern high-latitude location from Δ_{47} analysis alone (Vickers et al., 2019). However, without having any independent constraints on the true formation temperature of 66–465, we cannot rule out that the belemnite sample plots fortuitously indistinguishable from clumped isotope equilibrium, like it is observed for the brachiopod (Fig. 6a, c). If internal equilibrium were attained it could mean that heterogeneous oxygen isotope equilibrium has been reached as well. If so, the temperature dependence of the equilibrium oxygen isotope fractionation between $CaCO_3$ and H_2O of Daëron et al. (2019) should be used rather than the equation provided by Kim and O'Neil (1997) to calculate the $\delta^{18}O$ of the seawater the belemnite calcite crystallized from. A seawater-$\delta^{18}O$ value of −0.8 ± 0.6‰ is then obtained which is in better agreement with an ice-free world than the ~1‰ determined in the original study of Vickers et al. (2019). However, as shown on our experimental precipitate MD 1, a given carbonate can still exhibit negative departures from oxygen isotope equilibrium even when its dual clumped isotopic composition is indistinguishable from equilibrium. The reconstructed $\delta^{18}O$-value of −0.8 ± 0.6‰, therefore, represents a lowermost estimate of the seawater. Further investigations are necessary to identify if belemnites may have precipitated their calcite skeletons in homo- and heterogeneous isotopic equilibrium. Should belemnites represent equilibrium calcifiers, they could become ideal archives to reconstruct sea surface temperatures and seawater-$\delta^{18}O$ at high-precision. Note that the uncertainty of ±3 °C (2 SE) characteristic of sample 66–465 could likely be reduced if the number of replicate analyses is increased.

Finally, we acknowledge that the observation that relatively rapidly-precipitated carbonates such as the experimental precipitate MD 1 and the geothermal pipe carbonates apparently achieve dual clumped isotope equilibrium contradicts the earlier claims of Daëron et al. (2019), who concluded that there was a subtle but statistically significant difference in temperature-Δ_{47} regressions between biogenic samples and slow-growing calcites LGB 1 and DVH 1 (equivalent to LGB 2 and DVH 2 analyzed here). However, the recent analyses of LGB 2 and DVH 2 from the present study and that of Anderson et al. (2021) yield fully consistent I-CDES values, with virtually identical compositions for LGB 1 and LGB 2 but Δ_{47} values for DVH 2 about 8 ppm greater than originally reported for DVH 1 by Daëron et al. (2019). In light of the excellent
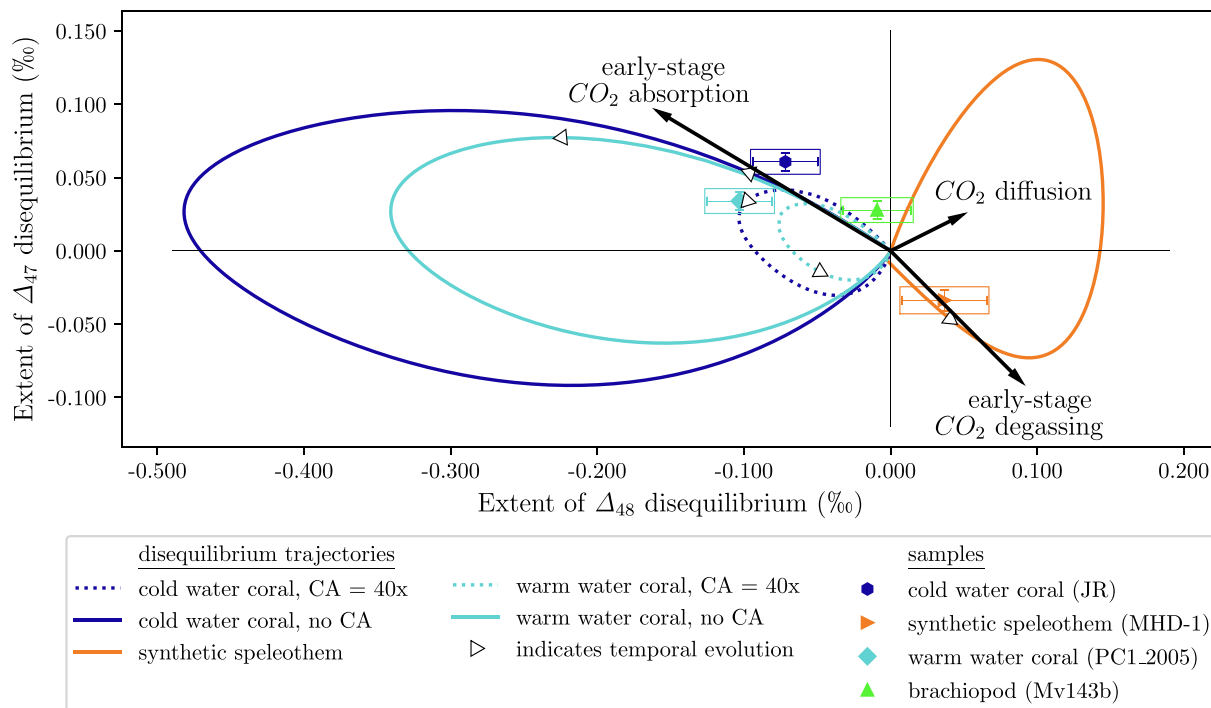
Fig. 7. Offsets of sample Δ_{47} (CDES) and Δ_{48} (CDES) (reprocessed from Bajnai et al., 2020) from equilibrium values predicted by known formation temperatures and Eqs. (5) and (6)). Temporal evolution of disequilibrium loops introduced by CO_2 absorption and CO_2 degassing kinetics were modeled for the conditions specific for the calcification of the warm water coral, cold water coral and speleothem-like samples (Bajnai et al., 2020). White arrows indicate the direction of temporal evolution of disequilibrium patterns and are positioned to mark t = 500 s and t = 170 s in the CO_2 absorption and CO_2 degassing model simulation, respectively. Linear vectors indicative of kinetics introduced during the early stages of CO_2 absorption (slope −0.6) and CO_2 degassing (slope −1.0) at the conditions specific for the investigated samples (Bajnai et al. (2020) and during diffusion (slope 0.5; Guo, 2020) are shown along with the samples. Boxes represent propagated 2 SE uncertainties, considering both the 2 SE characteristic of a sample (Table 3) and the 95 % confidence uncertainty of the calibration regression lines (Fig. 4a, b) specific for the temperature of sample formation. For further discussion see text.

agreement between DHC2-8 and DVH 2 observed here, it appears unlikely that this discrepancy can be attributed to heterogeneity between DVH 1 and DVH 2. We propose instead that the findings of Daëron et al. (2019) suffered from (1) the lack of ETH 4 analyses, leading to DVH 1 plotting well outside of the "anchor triangle" of ETH 1/2/3, thus increasing standardization errors (Daëron, 2021), and (2) an ill-advised attempt to extrapolate biogenic calibrations constrained between 0 and 25 °C to the 33.7 °C temperature of Devils Hole. In light of these new results, we thus conclude that the latest evidence clearly supports the hypothesis that carbonates precipitated from equilibrated DIC pools can be described, within current analytical precision limits, by a single Δ_{47} – T relationship over a wide range of crystallization rates.

5.5. Evidence for anti-clumped Δ_{48}

We have also analyzed the dual clumped isotopic composition of an industrially precipitated carbonate (Precarb 100) from Schaefer-Kalk, Germany, consisting of 99% $CaCO_3$ and 0.8% $MgCO_3$ (GU 1). Its technical production includes three steps: 1) decarboxylation of a 380 Ma year old calcite of marine sedimentary origin; 2) production of a $Ca(OH)_2$-saturated solution by the addition of meteoric water to CaO; 3) injection of carbonate-derived CO_2 into the $Ca(OH)_2$-saturated solution, evoking hydroxylation of CO_2 and instantaneous precipitation of $CaCO_3$. Decarboxylation temperature and the temperature of CO_2 injection are not made available by the company. As a result of the strong unidirectionality involved in its formation, GU 1 plots far away from the equilibrium line (Fig. 6a). It exhibits a negative Δ_{48} value (i.e., an anti-clumped composition; Δ_{48} (CDES 90) = $-0.419 \pm 0.016\text{‰}$, Table 1). This anti-clumping effect is consistent with previous model simulation results for CO_2 hydroxylation, which predict −0.928‰ depletion in the Δ_{64} (i.e. Δ_{48}) of HCO_3^- produced by hydroxylation compared to the expected equilibrium value at 25 °C (Guo, 2020). According to the hydroxylation reaction, 2/3 of the oxygen in the precipitated $CaCO_3$ will derive from CO_2, whereas 1/3 originates from dissolved OH^-. The two oxygen pools have very likely different oxygen isotopic compositions. CO_2 deriving from the pyrolysis of $CaCO_3$ has a $\delta^{18}O$ value very similar (up to 3‰ lower) to that of the starting carbonate (Miller et al., 2002). At ambient temperatures characteristic of the marine realm, the oxygen isotope fractionation between calcite and water (1000lnα($CaCO_3$-H_2O)) is 25–30‰ (e.g., Kim and O'Neil, 1997; Daëron et al., 2019).

Therefore, the CO_2 deriving from the decarboxylation likely has a positive $\delta^{18}O_{VSMOW}$ value. On the contrary, dissolved OH^- can be expected to have a negative $\delta^{18}O_{VSMOW}$ value. Its oxygen originates from meteoric water and the hydroxyl-water fractionation is likely negative (Green and Taube, 1963; Zeebe, 2020). When CO_2 and OH^- react to form bicarbonate, kinetic isotope effects (KIE's) also need to be considered. These are predicted to further increase the isotopic difference between the two oxygen pools grouping together in the bicarbonate, provided CO_2 and OH^- are available in unrestricted amounts such that $\delta^{18}O$ of both the CO_2 and OH^- remain unaffected by Rayleigh removal (Guo and Zhou, 2019b). Theory predicts an anti-clumped Δ_{64} value can result for the dissolved bicarbonate when its indistinguishable oxygen atoms are sourced from two or more isotopically different pools (Yeung, 2016; Röckmann et al., 2016). The negative Δ_{64} value largely results from the fact that the apparent stochastic 64/60 ratio calculated from the measured bulk oxygen isotope abundance does not correspond to the true stochastic 64/60 ratio of the bicarbonate. The apparent Δ_{64} value of the bicarbonate is defined as

$$\Delta_{64} = \frac{\left(\frac{64}{60}\right)}{\left(\frac{64}{60}\right)^*} - 1 \tag{7}$$

where $\left(\frac{64}{60}\right)$ represents the measured 64/60 ratio of the bicarbonate and $\left(\frac{64}{60}\right)^*$ its apparent stochastic ratio calculated from the measured bulk oxygen isotope abundance $^{18}R_{av}$. $^{18}R_{av}$ represents the average over all three oxygens in the bicarbonate. For the calculation of the true stochastic 64/60 ratio knowledge of the isotopic compositions of each of the three oxygen sources that combine in the bicarbonate is required. The true $\Delta_{64,t}$ value of the bicarbonate is defined as follows

$$\Delta_{64,t} = \frac{\left(\frac{64}{60}\right)}{\left(\frac{64}{60}\right)^{**}} - 1 \tag{8}$$

where $\left(\frac{64}{60}\right)^{**}$ represents the true stochastic 64/60 ratio of the bicarbonate which considers the isotopic compositions ($^{18}R_i$) of each of the individual oxygen pools (i) grouping together in the bicarbonate. The apparent stochastic 64/60 ratio calculated from the bulk ^{18}O abundance ($^{18}R_{av}$) will always be more positive than the true stochastic 64/60 ratio if the three indistinguishable oxygen atoms in the bicarbonate do not derive from the same oxygen pool (Röckmann et al., 2016). The statistical anomaly that results from this mathematical artifact can be expressed as $\Delta_{64, st}$, i.e. by normalizing the true stochastic 64/60 ratio to the apparent stochastic 64/60 ratio:

$$\Delta_{64,st} = \frac{\left(\frac{64}{60}\right)^{**}}{\left(\frac{64}{60}\right)^*} - 1 \tag{9}$$

with

$$\frac{\left(\frac{64}{60}\right)^{**}}{\left(\frac{64}{60}\right)^*} \simeq \frac{3(R_1 R_2 + R_1 R_3 + R_2 R_3)}{(R_1 + R_2 + R_3)^2} \tag{10}$$

If the three oxygen sources constituting the bicarbonate do not have identical isotopic compositions, a negative statistical value is obtained for $\Delta_{64, st}$. With respect to the

hydroxylation of CO_2, the absolute value of $\Delta_{64, st}$ depends on the difference in the isotopic compositions of the two pools (CO_2, OH^-) of oxygen constituting the bicarbonate. Multiplication of (8) and (9) and consideration of (7) gives

$$\Delta_{64} = \Delta_{64, st} + \Delta_{64, t} + \Delta_{64, st}\,\Delta_{64, t} \tag{11}$$

At the high pH value characteristic of a $Ca(OH)_2$-saturated solution, the dissolved bicarbonate produced by the hydroxylation reaction is completely converted to dissolved carbonate which, in a subsequent step, is quantitatively removed from the solution as calcite. Eq. (11) should, therefore, also be valid for the precipitated calcite. The $\Delta_{48} - \Delta_{64}$ fractionation factor characteristic of phosphoric acid digestion at 90 °C is 0.124‰, as becomes evident from equation (6). Considering that the product of $\Delta_{64, st}$ and $\Delta_{64, t}$ is negligibly small relative to their sum, we obtain:

$$\Delta_{48} \simeq \Delta_{64, st} + \Delta_{64, t} + 0.000124 \tag{12}$$

Eq. (12) demonstrates that the evolved CO_2 will carry an anti-clumped Δ_{48} value if the absolute (negative) $\Delta_{64, st}$ anomaly is larger than the sum of $\Delta_{64, t} + 0.000124$. No such combinatorial effect prevails on the Δ_{63} value of the bicarbonate or the calcite, respectively, as double heavy isotope substitution in $^{13}C^{18}O^{16}O^{16}O$ accompanies two different elements (Röckmann et al., 2016; Yeung, 2016).

Note that the oxygen isotopic compositions of the two oxygen pools grouping together in the GU 1 precursor bicarbonate cannot be determined directly from the measured Δ_{48} value since $\Delta_{64, t}$ is unknown. However, based on the measured Δ_{47} and Δ_{48} values of GU 1 of 0.226‰ and −0.419‰, respectively (Table 1), we can simulate the isotope fractionation during its formation using IsoDIC (Guo, 2020). Assuming the isotope composition of GU 1
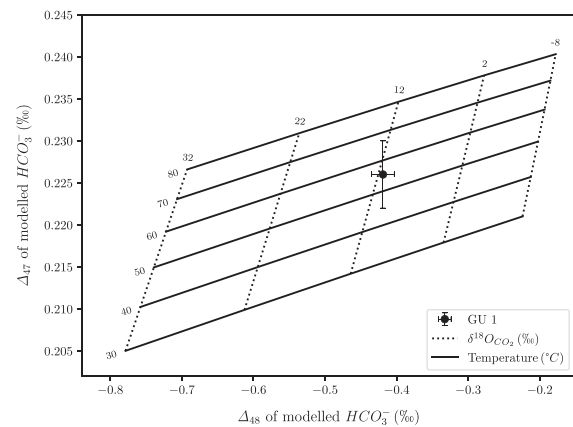

Fig. 8. Model calculations of Δ_{47} and Δ_{48} for GU 1 using IsoDIC (Guo, 2020). Measured Δ_{47} and Δ_{48} of GU 1 become consistent with modeled values if the CO_2 deriving from decarboxylation of calcite had a $\delta^{18}O$ of ~12‰ and the $Ca(OH)_2$ solution a temperature of ~55 °C. The best-fit Δ_{47} and Δ_{48} values of the CO_2 corresponded to equilibrium at ~300 °C (not shown). We further assumed that the oxygen isotopic composition of the Ca$(OH)_2$ was buffered by local meteoric water ($\delta^{18}O$ of ~−8‰, Stumpp et al., 2014).

directly reflects the isotopic composition of HCO_3^- produced by CO_2 hydroxylation, Δ_{47} and Δ_{48} of GU 1 are most consistent with the hydroxylation of CO_2 with local meteoric water ($\delta^{18}O_{water}$ assumed to $-8‰$, Stumpp et al., 2014) at ~55 °C, with a CO_2 isotopic composition of $\delta^{18}O_{CO2} = ~12‰$ and clumped isotopically equilibrated at 300 °C (Fig. 8). According to the IsoDIC simulation, the difference in the isotopic compositions of the two oxygen pools grouping together in the bicarbonate is ~62.5‰ (considering KIE's of Guo and Zhou, 2019b), corresponding to a $\Delta_{64, st}$ of ~$-0.44‰$ (Eq. (10)) and a $\Delta_{64, t}$ of ~$-0.10‰$ (Eq. (12)).

6. CONCLUSIONS

We have analyzed the dual clumped isotopic composition of two slowly grown natural calcites (Laghetto Basso, Devils Hole), five hydrothermally precipitated calcites and three calcites internally equilibrated at high temperatures. Previous oxygen isotope analyses on the investigated natural and hydrothermal calcites implied that heterogeneous isotopic equilibrium was closely attained in these samples. Anchoring dual clumped isotope data to the same reference frame (CDES 90), we obtain $\Delta_{47} - \Delta_{48}$ - T relationships whose accuracy is independently confirmed by geothermal pipe carbonates and an experimentally precipitated carbonate. Based on the proposed equilibrium relationship we confirm that CO_2 absorption and CO_2 degassing kinetics play a pivotal role in governing the isotopic composition of corals and speleothems. Dual clumped isotope analysis of carbonates represents a promising and powerful new tool (i) to investigate the nature and extent of kinetics involved in primary and secondary carbonate (bio)mineralization, (ii) to reconstruct accurate (paleo)temperatures devoid of a kinetic bias and (iii) to explore the isotopic heterogeneity of oxygen pools contributing to carbonate formation. In the low temperature range, precisions $\leq \pm 3$ °C can be achieved on the 95% confidence interval level, provided the investigated carbonate attained internal isotopic equilibrium.

Declaration of Competing Interest

The authors declare that they have no known competing financial interests or personal relationships that could have appeared to influence the work reported in this paper.

APPENDIX A. SUPPLEMENTARY MATERIAL

Supplementary data to this article can be found online at https://doi.org/10.1016/j.gca.2021.07.012.

REFERENCES

Anderson N. T., Kelson J. R., Kele S., Daëron M., Bonifacie M., Horita J., Mackey T. J., John C. M., Kluge T., Petschnig P., Jost A. B., Huntington K. W., Bernasconi S. M. and Bergmann K. D. (2021) A unified clumped isotope thermometer calibration (0.5 – 1100 °C) using carbonate-based standardization (2021). *Geophys Res. Lett* **48**, e2020GL092069.

Bajnai D., Fiebig J., Tomašovych A., Milner G. S., Rollion-Bard C., Raddatz J., Löffler N., Primo-Ramos C. and Brand U. (2018) Assessing kinetic fractionation in brachiopod calcite using clumped isotopes. *Sci. Rep.* **8**, 533.

Bajnai D., Guo W., Spoetl C., Coplen T. B., Methner K., Löffler N., Krsnik E., Gischler E., Hansen M., Henkel D., Price G. D., Raddatz J., Scholz D. and Fiebig J. (2020) Dual clumped isotope thermometry resolves kinetic biases in carbonate formation temperatures. *Nat. Commun.* **11**, 4005.

Bernasconi S. M., Müller I. A., Bergmann K. D., Breitenbach S. F. M., Fernandez A., Hodell D. A., Jaggi M., Meckler A. N., Millan I. and Ziegler M. (2018) Reducing uncertainties in carbonate clumped isotope analysis through consistent carbonate-based standardization. *Geochem. Geophys. Geosyst.* **19**, 2895–2914.

Bernasconi S. M., Daëron M., Bergmann K. D., Bonifacie M., Meckler A. N., Affek H. P., Anderson N., Bajnai D., Barkan E., Beverly E., Blamart D., Burgener L., Calmels D., Chaduteau C., Clog M., Davidheiser-Kroll B., Davies A., Dux F., Eiler J. M., Elliott B., Fetrow C., Fiebig J., Goldberg S., Hermoso M., Huntington K. W., Hyland E., Ingalls M., Jaggi M., John C. M., Jost A. B., Katz S., Kelson J., Kluge T., Kocken I. J., Laskar A., Leutert T. J., Liang D., Lucarelli J., Mackey T. J., Mangenot X., Meinicke N., Modestou S. E., Müller I. A., Murray S., Neary A., Packard N., Passey B. H., Pelletier E., Petersen S., Piasecki A., Schauer A., Snell K. E., Swart P. K., Tripati A., Upadhyay D., Vennemann T., Winkelstern I., Yarian D., Yoshida N., Zhang N. and Ziegler M. (2021) InterCarb: A community effort to improve interlaboratory standardization of the carbonate clumped isotope thermometer using carbonate standards. *Geochem. Geophys. Geosyst.*.

Bonifacie M., Calmels D., Eiler J. M., Horita J., Chaduteau C., Vasconcelos C., Agrinier P., Katz A., Passey B. H., Ferry J. M. and Bourrand J. J. (2017) Calibration of the dolomite clumped isotope thermometer from 25 to 350 °C, and implications for a universal calibration for all (Ca, Mg, Fe)CO_3 carbonates. *Geochim. Cosmochim. Acta* **200**, 255–279.

Bristow T. F., Bonifacie M., Derkowski A., Eiler J. M. and Grotzinger J. P. (2011) A hydrothermal origin for isotopically anomalous cap dolostone cements from south China. *Nature* **474**, 68–71.

Cohen A. L. and McConnaughey T. A. (2003) Geochemical perspectives on coral mineralization. *Rev. Mineral. Geochem.* **54**, 151–187.

Coplen T. B. (2007) Calibration of the calcite–water oxygen-isotope geothermometer at Devils Hole, Nevada, a natural laboratory. *Geochim. Cosmochim. Acta* **71**, 3948–3957.

Daëron M. (2021) Full propagation of analytical uncertainties in Δ_{47} measurements. *Geochem. Geophys. Geosyst.*.

Daëron M., Guo W., Eiler J., Genty D., Blamart D., Boch R., Drysdale R., Maire R., Wainer K. and Zanchetta G. (2011) $^{13}C^{18}O$ clumping in speleothems: Observations from natural caves and precipitation experiments. *Geochim. Cosmochim. Acta* **75**, 3303–3317.

Daëron M., Blamart D., Peral M. and Affek H. P. (2016) Absolute isotopic abundance ratios and the accuracy of Δ_{47} measurements. *Chem. Geol.* **442**, 83–96.

Daëron M., Drysdale R. N., Peral M., Huyghe D., Blamart D., Coplen T. B., Lartaud F. and Zanchetta G. (2019) Most Earth-surface calcites precipitate out of isotopic equilibrium. *Nat. Commun.* **10**, 1–7.

Dennis K. J. and Schrag D. P. (2010) Clumped isotope thermometry of carbonatites as an indicator of diagenetic alteration. *Geochim. Cosmochim. Acta* **74**, 4110–4122.

Dennis K. J., Affek H. P., Passey B. H., Schrag D. P. and Eiler J. M. (2011) Defining an absolute reference frame for clumped isotope studies of CO_2. *Geochim. Cosmochim. Acta* **75**, 7117–7131.

Devriendt L. S., Watkins J. M. and McGregor H. V. (2017) Oxygen isotope fractionation in the $CaCO_3$–DIC–H_2O system. *Geochim. Cosmochim. Acta* **214**, 115–142.

Dietzel M., Gussone N. and Eisenhauer A. (2004) Co-precipitation of Sr^{2+} and Ba^{2+} with aragonite by membrane diffusion of CO_2 between 10 and 50 °C. *Chem. Geol.* **203**, 139–151.

Drysdale R. N., Bence T. P., Hellstrom J. C., Couchoud I., Greig A., Bajo P., Zanchetta G., Isola I., Spoetl C., Baneschi I., Regattieri E. and Woodhead J. D. (2012) (2012) Precise microsampling of poorly laminated speleothems for U-series dating. *Quat. Geochronol.* **14**, 38–47.

Eagle R. A., Tutken T., Martin T. S., Tripati A. K., Fricke H. C., Connely M., Cifelli R. L. and Eiler J. M. (2011) Dinosaur body temperatures determined from isotopic (^{13}C–^{18}O) ordering in fossil biominerals. *Science* **333**, 443–445.

Epstein S., Buchsbaum R., Lowenstam H. A. and Urey H. C. (1953) Revised carbonate-water isotopic temperature scale. *Geol. Soc. Am. Bull.* **64**, 1315–1326.

Fernandez A., Müller I. A., Rodríguez-Sanz L., van Dijk J., Looser N. and Bernasconi S. M. (2017) A reassessment of the precision of carbonate clumped isotope measurements: Implications for calibrations and paleoclimate reconstructions. *Geochem. Geophys. Geosyst.* **18**, 4375–4386.

Fiebig J., Bajnai D., Löffler N., Methner K., Krsnik E., Mulch A. and Hofmann S. (2019) Combined high-precision Δ_{48} and Δ_{47} analysis of carbonates. *Chem. Geol.* **522**, 186–191.

Friedman I. and O'Neil J. R. (1977) Compilation of stable isotope fractionation factors of geochemical interest, Data of Geochemistry, Geochemical Survey Professional Paper 440-KK6th edition. KK1–KK12.

Ghosh P., Adkins J., Affek H., Balta B., Guo W., Schauble E. A., Schrag D. and Eiler J. M. (2006) ^{13}C–^{18}O bonds in carbonate minerals: A new kind of paleothermometer. *Geochim. Cosmochim. Acta* **70**, 1439–1456.

Green M. and Taube H. (1963) Isotopic fractionation in the OH-H_2O exchange reaction. *J. Phys. Chem.* **67**, 1565–1566.

Guo W. and Eiler J. M. (2007) Temperatures of aqueous alteration and evidence for methane generation on the parent bodies of the CM chondrites. *Geochim. Cosmochim. Acta* **71**, 5565–5575.

Guo W. and Zhou C. (2019a) Patterns and controls of disequilibrium isotope effects in speleothems: Insights from an isotope-enabled diffusion-reaction model and implications for quantitative thermometry. *Geochim. Cosmochim. Acta* **267**, 196–226.

Guo W. and Zhou C. (2019b) Triple oxygen isotope fractionation in the DIC-H_2O-CO_2 system: A numerical framework and its implications. *Geochim. Cosmochim. Acta* **246**, 541–564.

Guo W. (2020) Kinetic clumped isotope fractionation in the DIC-H_2O-CO_2 system: Patterns, controls, and implications. *Geochim. Cosmochim. Acta* **268**, 230–257.

Hill P. S., Tripati A. K. and Schauble E. A. (2014) Theoretical constraints on the effects of pH, salinity, and temperature on clumped isotope signatures of dissolved inorganic carbon species and precipitating carbonate minerals. *Geochim. Cosmochim. Acta* **125**, 610–652.

Huntington K. W., Budd D. A., Wernicke B. P. and Eiler J. M. (2011) Use of clumped-isotope thermometry to constrain the crystallization temperature of diagenetic calcite. *J. Sediment. Res.* **81**, 656–669.

Jautzy J. J., Savard M. M., Dhillon R. S., Bernasconi S. M. and Smirnoff A. (2020) Clumped isotope temperature calibration for calcite: Bridging theory and experimentation. *Geochem. Perspect. Lett.* **14**, 36–41.

Kelson J. R., Huntington K. W., Schauer A., Saenger C. and Lechler A. R. (2017) Toward a universal carbonate clumped isotope calibration: Diverse synthesis and preparatory methods suggest a single temperature relationship. *Geochim. Cosmochim. Acta* **197**, 104–131.

Kim S.-T. and O'Neil J. R. (1997) Equilibrium and nonequilibrium oxygen isotope effects in synthetic carbonates. *Geochim. Cosmochim. Acta* **61**, 3461–3475.

Kim S. T., Mucci A. and Taylor B. E. (2007) Phosphoric acid fractionation factors for calcite and aragonite between 25 and 75 °C: Revisited. *Geochim. Cosmochim. Acta* **246**, 135–146.

Kluge T., John C. M., Boch R. and Kele S. (2018) Assessment of factors controlling clumped isotopes and $\delta^{18}O$ values of hydrothermal vent calcites. *Geochem. Geophys. Geosyst.* **19**, 1844–1858.

Levitt N. P., Eiler J. M., Romanek C. S., Beard B. L., Xu H. and Johnson C. M. (2018) Near equilibrium ^{13}C–^{18}O bonding during inorganic calcite precipitation under chemo-stat conditions. *Geochem. Geophys. Geosyst.* **19**, 901–920.

Merritt D. A. and Hayes J. M. (1994) Factors controlling precision and accuracy in isotope-ratio-monitoring mass spectrometry. *Anal. Chem.* **66**, 2336–2347.

Miller M. F., Franchi I. A., Thiemens M. H., Jackson T. L., Brack A., Kurat G. and Pillinger C. T. (2002) Mass-independent fractionation of oxygen isotopes during thermal decomposition of carbonates. *Proc. Natl. Acad. Sci. USA* **99**, 10988–10993.

Niedermayr A., Köhler S. J. and Dietzel M. (2013) Impacts of aqueous carbonate accumulation rate, Magnesium and polyaspartic acid on calcium carbonate formation (6–40 °C). *Chem. Geol.* **340**, 105–120.

Nürnberg D., Bijma J. and Hemleben C. (1996) Assessing the reliability of magnesium in foraminiferal calcite as a proxy for water mass temperatures. *Geochim. Cosmochim. Acta* **60**, 803–814.

O'Neil J. R., Clayton R. N. and Mayeda T. K. (1969) Oxygen isotope fractionation in divalent metal carbonates. *J. Chem. Phys.* **51**, 5547–5558.

Passey B. H., Levin N. E., Cerling T. E., Brown F. H. and Eiler J. M. (2010) High temperature environments of human evolution in East Africa based on bond ordering in paleosol carbonates. *Proc. Natl. Acad. Sci. USA* **107**, 11245–11249.

Passey B. H. and Henkes G. A. (2012) Carbonate clumped isotope bond reordering and geospeedometry. *Earth Planet. Sci. Lett.* **351–352**, 223–236.

Peral M., Daëron M., Blamart D., Bassinot F., Dewilde F., Smialkowski N., Isguder G., Bonnin J., Jorissen F., Kissel C., Michel E., Vazquez R. N. and Waelbroeck C. (2018) Updated

calibration of the clumped isotope thermometer in planktonic and benthic foraminifera. *Geochim. Cosmochim. Acta* **239**, 1–16.

Petersen S. V., Defliese W. F., Saenger C., Daëron M., Huntington K. W., John C. M., Kelson J. R., Bernasconi S. M., Colman A. S., Kluge T., Olack G. A., Schauer A. J., Bajnai D., Bonifacie M., Breitenbach S. F. M., Fiebig J., Fernandez A. B., Henkes G. A., Hodell D., Katz A., Kele S., Lohmann K. C., Passey B. H., Peral M. Y., Petrizzo D. A., Rosenheim B. E., Tripati A., Venturelli R., Young E. D. and Winkelstern I. Z. (2019) Effects of improved ^{17}O correction on inter-laboratory agreement in clumped isotope calibrations, estimates of mineral-specific offsets, and temperature dependence of acid digestion fractionation. *Geochem. Geophys. Geosyst.* **20**, 3495–3519.

Plummer L. N., Busenberg E. and Riggs A. C. (2000) In-situ growth of calcite at Devils Hole, Nevada: comparison of field and laboratory rates to a 500,000 year record of near-equilibrium calcite growth. *Aquat. Geochem.* **6**, 257–274.

Röckmann T., Popa M. E., Krol M. C. and Hofmann M. E. G. (2016) Statistical clumped isotope signatures. *Sci. Rep.* **6**, 31947.

Saenger C., Affek H. P., Felis T., Thiagarajan N., Lough J. M. and Holcomb M. (2012) Carbonate clumped isotope variability in shallow water corals: Temperature dependence and growth-related vital effects. *Geochim. Cosmochim. Acta* **99**, 224–242.

Schmid T. W. and Bernasconi S. M. (2010) An automated method for 'clumped-isotope' measurements on small carbonate samples. *Rap. Commun. Mass Spectrom.* **24**, 1955–1963.

Schouten S., Hopmans E. C., Schefuß E. and Sinninghe Damsté J. S. (2002) Distributional variations in marine crenarchaeotal membrane lipids: a new tool for reconstructing ancient sea water temperatures?. *Earth Planet Sci. Lett.* **204**, 265–274.

Stumpp C., Klaus J. and Stichler W. (2014) Analysis of long-term stable isotopic composition in German precipitation. *J. Hhydrol.* **517**, 351–361.

Swart P. K., Murray S. T., Staudigel P. T. and Hodell D. A. (2019) Oxygen isotopic exchange between CO_2 and phosphoric acid: Implications for the measurement of clumped isotopes in carbonates. *Geochem. Geophys. Geosyst.* **20**, 3730–3750.

Tang J., Dietzel M., Fernandez A., Tripati A. K. and Rosenheim B. E. (2014) Evaluation of kinetic effects on clumped isotope fractionation (Δ_{47}) during inorganic calcite precipitation. *Geochim. Cosmochim. Acta* **134**, 120–136.

Tripati A. K., Hill P. S., Eagle R. A., Mosenfelder J. L., Tang J., Schauble E. A., Eiler J. M., Zeebe R. E., Uchikawa J., Coplen T. B., Ries J. B. and Henry D. (2015) Beyond temperature: clumped isotope signatures in dissolved inorganic carbon species and the influence of solution chemistry on carbonate mineral composition. *Geochim. Cosmochim. Acta* **166**, 344–371.

Urey H. C. (1947) The thermodynamic properties of isotopic substances. *J. Chem. Soc.* **0**, 562–581.

Veizer J. and Prokoph A. (2015) Temperatures and oxygen isotopic composition of Phanerozoic oceans. *Earth Sci. Rev.* **146**, 92–104.

Vickers M. L., Bajnai D., Price G. D., Linckens J. and Fiebig J. (2019) Southern high-latitude warmth during the Jurassic-Cretaceous: New evidence from clumped isotope thermometry. *Geology* **47**, 724–728.

Wang Z., Schauble E. A. and Eiler J. M. (2004) Equilibrium thermodynamics of multiply substituted isotopologues of molecular gases. *Geochim. Cosmochim. Acta* **68**, 4779–4797.

Watkins J. M., Hunt J. D., Ryerson F. J. and DePaolo D. J. (2014) The influence of temperature, pH, and growth rate on the δ^{18}O composition of inorganically precipitated calcite. *Earth Planet. Sci. Lett.* **404**, 332–343.

Watkins J. M. and Hunt J. D. (2015) A process-based model for non-equilibrium clumped isotope effects in carbonates. *Earth Planet. Sci. Lett.* **432**, 152–165.

Yeung L. Y. (2016) Combinatorial effects on clumped isotopes and their significance in biogeochemistry. *Geochim. Cosmochim. Acta* **172**, 22–38.

Zeebe R. E. (1999) An explanation of the effect of seawater carbonate concentration on foraminiferal oxygen isotopes. *Geochim. Cosmochim. Acta* **63**, 2001–2007.

Zeebe R. E. (2020) Oxygen isotope fractionation between water and the aqueous hydroxide ion. *Geochim. Cosmochim. Acta* **289**, 182–195.

Associate editor: Cedric Michael John